Thickness-Dependent Plasma Activation in Binder-Free Multilayer Ni-Co-O Anodes for Alkaline Oxygen Evolution

Mohit Chatwani, Christian Marcks, Christina Meinert, Ioannis Spanos, Adarsh Jain,
Viktor Mackert, Ahammed Suhail Odungat, Timo Wagner, Lars Grebener, Abhishek Shaji,
Hao Yun, Mena-Alexander Kräenbring, Nicolas Wöhrl, Anna K. Mechler,
Vineetha Vinayakumar, Doris Segets[*]

M. Chatwani, A. Jain, L. Grebener, A. S. Odungat, A. Shaji, H. Yun, M. A. Kräenbring,
Dr. V. Vinayakumar, Prof. Dr. D. Segets
Institute for Energy and Materials Processes – Particle Science and Technology (EMPI-PST)
University of Duisburg-Essen
Carl-Benz-Straße 199, 47057 Duisburg (Germany)
E-mail: doris.segets@uni-due.de

Dr. N. Wöhrl, Dr. V. Vinayakumar, Prof. Dr. D. Segets
Center for Nanointegration Duisburg-Essen (CENIDE)
University of Duisburg-Essen
Carl-Benz-Straße 199, 47057 Duisburg (Germany)

C. Meinert, Dr. T. Wagner, Dr. N. Wöhrl
Faculty of Physics
University of Duisburg-Essen
Carl-Benz-Straße 199, 47057 Duisburg (Germany)

C. Marcks, Prof. Dr. A. K. Mechler
Electrochemical Reaction Engineering (AVT.ERT)
RWTH Aachen University
Forckenbeckstraße 51, 52074 Aachen (Germany)

Prof. Dr. A. K. Mechler
Institute of Energy Technologies, Electrochemical Process Engineering (IET-4)
Forschungszentrum Jülich GmbH
Wilhelm-Johnen-Straße, 52428 Jülich (Germany)

Prof. Dr. A. K. Mechler
Jülich Aachen Research Alliance (JARA)
Forckenbeckstraße 51, 52074 Aachen (Germany)

Dr. I. Spanos
Heterogeneous Reactions
Max Planck Institute for Chemical Energy Conversion
Stiftstr. 34-36, 45470 Mülheim an der Ruhr (Germany)

Dr. V. Mackert
The Hydrogen and Fuel Cell Center (ZBT GmbH)
Carl-Benz-Straße 201, 47057 Duisburg (Germany)

Keywords: binder-free, alkaline water electrolysis, plasma treatment, ultrasonic spray coating, catalyst layer, mechanical stability

Binder-free Ni-Co-O anodes were fabricated by ultrasonic spray-coating multilayer catalyst films directly onto Ni substrates, followed by nitrogen plasma treatment to enhance performance in alkaline water electrolysis. By systematically varying coating thickness, we were able to elucidate the relationship between plasma-induced surface reconstruction and electrode architecture. Plasma exposure, with an effective modification depth of approximately 1 μm, promoted near-surface cobalt enrichment and improved wettability while preserving the bulk crystal structure, as confirmed by X-ray photoelectron spectroscopy, energy-dispersive X-ray spectroscopy, and grazing-incidence X-ray diffraction. Despite this only partial activation of thicker coatings, their enhanced porosity and micro-scale roughness facilitated superior electrolyte penetration and gas release, leading to higher catalytic efficiency. Consequently, the thickest plasma-treated electrode exhibits an overpotential of 335 mV at 100 mA cm^{-2} in 1 M KOH, outperforming the Ni substrate reference (380 mV), while maintaining robust mechanical integrity without delamination. These findings demonstrate that catalytic performance depends on the interplay between finite plasma activation depth and multilayer thickness, highlighting the need to tailor coating thickness to balance surface modification with effective electrolyte penetration and gas transport. Nitrogen plasma treatment thus provides a scalable strategy for engineering mechanically robust and efficient binder-free Ni-Co-O anodes for alkaline OER.

1. Introduction

The increasing global energy demand over recent decades has led to the extensive exploitation of non-renewable fossil fuels, contributing significantly to carbon emissions and accelerating climate change[1–3]. While renewable energy sources such as solar and wind power offer viable alternatives, their intermittent nature poses challenges for a stable energy supply. Consequently, electrochemical energy storage and conversion technologies, including supercapacitors, batteries, and hydrogen-based systems, provide promising pathways for efficient and flexible energy utilization[4]. Among these, hydrogen has gained considerable attention as a clean energy carrier, and its production technologies have witnessed rapid development in recent years[5]. Compared with proton exchange membrane (PEM) electrolysis, which exhibits similar technology readiness levels, and the emerging anion exchange membrane (AEM) technology, alkaline water electrolysis (AWE) remains a cost-effective and widely implemented approach for large-scale green hydrogen production[6]. However, the overall efficiency is limited by kinetic losses at both the anode and the cathode, manifested as overpotentials, with the oxygen evolution reaction (OER) at the anode representing the dominant contribution due to its intrinsically sluggish multi-electron transfer mechanism[7,8]. To address this limitation, various transition-metal-based oxides, particularly those containing Ni and Co, have been employed as electrocatalysts to reduce kinetic barriers[9]. Despite their favorable activity and stability in alkaline media, these catalysts are typically integrated into electrodes using polymeric binders to enhance mechanical adhesion[10,11]. However, this approach introduces additional cost, impairs electronic conductivity, and often involves per- and polyfluoroalkyl substances (PFAS), which are associated with environmental and health concerns[12]. Moreover, the incorporation of polymeric binders increases formulation complexity by introducing an additional component that must be optimized alongside the catalyst and solvent system, which may limit scalability for large-area electrode fabrication[13].

To circumvent these limitations, binder-free electrode fabrication strategies have gained increasing interest[14,15]. Unlike conventional binder-based systems, these electrodes rely on direct physical or chemical bonding between the catalyst layer and the conductive substrate, thereby eliminating polymer-induced interfacial resistance and establishing continuous electronic pathways for efficient charge transfer. However, they often involve complex synthesis steps or limited structural control. For example, hierarchical NiCoSe or NiFeCo oxide nanostructures grown hydrothermally on Ni foam demonstrated a high activity but require multistep processing and yield mechanically fragile coatings[16]. Defect-engineered and heterostructured catalysts such as Fe-doped NiCoP or Co_3O_4/Fe_2O_3 composites, can achieve OER overpotentials below 260 mV at 10 mA cm^{-2} (referenced to the thermodynamic potential of 1.23 V vs. RHE), but reproducibility and thickness scalability remain challenging[17]. Similarly, rapid roll-to-roll or electrodeposition routes enable binder-free coatings with reasonable performance[18–20], yet lack precise control over layer thickness and chemical uniformity. In our previous work[14], mechanochemical activation of NiO powder represented another scalable strategy to enhance the intrinsic catalytic activity prior to deposition and to produce binder-free electrodes. However, this approach remains at an early stage of maturity. Another, overlooked strategy that provides additional opportunities to tailor interfacial chemistry and electrode architecture is post-deposition surface engineering by plasma treatment[21]. Recently we uncovered that plasma exposure can induce defect formation, compositional redistribution, and electrode surface reconstruction without altering the overall electrode geometry or requiring complex synthesis steps[22]. Wagner et al.[23] demonstrated that N_2 plasma treatment can restructure Ni surfaces, enhancing their reactivity and wettability, while Vinayakumar et al.[24] showed that the same treatment removes fluorine residues from Nafion-containing electrodes, reducing the OER overpotential by 43 mV at 100 mA cm^{-2} in 1 M KOH compared to untreated anodes.

However, while plasma activation is well established for thin films and monolayer catalysts, its penetration depth, thickness-dependent reconstruction, and mechanical implications in multilayer electrodes remain poorly understood. In particular, the extent to which plasma-induced modifications propagate within dense catalytic coatings and how such depth-limited activation governs interfacial adhesion, surface wettability, and catalytic function has not been quantitatively analyzed. This work addresses these gaps by systematically investigating thickness-dependent nitrogen plasma activation in spray-coated Ni-Co-O multilayers, correlating plasma penetration depth with chemical reconstruction, mechanical stability, and electrochemical performance.

To do so, we systematically investigate nitrogen plasma treatment of spray-coated multilayer Ni-Co-O anodes with controlled thickness. By combining depth-resolved compositional analysis, mechanical adhesion testing, operando Raman spectroscopy, and electrochemical evaluation, we elucidate how the plasma penetration depth interacts with film thickness to dictate chemical reconstruction and catalytic response. The thickest plasma-treated electrode achieves a clearly reduced overpotential of 335 mV at 100 mA cm^{-2} in 1 M KOH, significantly outperforming bare Ni while maintaining mechanical integrity. Beyond performance enhancement, this work establishes a mechanistic framework describing how a finite plasma-modification depth interacts with catalyst-layer thickness. The results demonstrate that the effectiveness of plasma activation is governed not only by surface chemistry but also by thickness-dependent changes in morphology, electrolyte accessibility, and interfacial stability, providing practical design guidelines for scalable binder-free alkaline electrolysis electrodes.

2. Results and discussion

To elucidate how depth-limited plasma activation interacts with the multilayer anodes of different thicknesses, a systematic experimental strategy was adopted as presented in **Figure 1**. The central objective of this study is to isolate intrinsic plasma-catalyst interactions in binder-free Ni-Co-O electrodes and to correlate plasma penetration depth with coating thickness, interfacial stability, and electrochemical response. In our previous study by Vinayakumar et al.[24], the Ni-Co-O catalyst was formulated with Nafion as a binder to enhance mechanical adhesion. In contrast, the present work deliberately eliminates the polymeric binder to avoid fluorine-related surface effects and to enable direct investigation of plasma-induced chemical reconstruction within the catalyst layer itself. This binder-free approach is essential to decouple plasma-material interactions from plasma-binder chemistry.

Transitioning to a binder-free formulation required re-optimization of the ink composition to ensure comparable dispersion stability and coating quality. Building upon the Hansen solubility parameter (HSP) analysis reported previously[24], an ethanol-water mixture was selected as the continuous phase for generating Ni-Co-O dispersions that enable homogeneous particle distribution and colloidal stability in the liquid, as well as cost-effective processing. The dispersion stability of the modified binder-free ink was verified by analytical centrifugation (**Figure S1**). The transmittogram[25] shows uniform sedimentation behavior without rapid agglomeration, indicating sufficient stability for spray deposition under gravity-driven conditions for approximately six days. This validation confirms that the removal of Nafion does not compromise formulation quality.

Using this optimized binder-free ink, Ni-Co-O electrodes were fabricated by ultrasonic spray coating with controlled layer deposition, specifically 40 layers (40L), 80 layers (80L), and 120 layers (120L). Each electrode set was then subjected to nitrogen plasma treatment (denoted PT-40L, PT-80L, PT-120L), enabling systematic comparison of plasma effects across distinct thickness scales.

The following sections elucidate the interdependence between ink-governed architecture of the coated anode layers, thickness-dependent plasma-material interactions, and surface-limited chemical reconstruction, and their combined impact on the physicochemical properties, mechanical integrity, and electrocatalytic performance of the generated anodes.

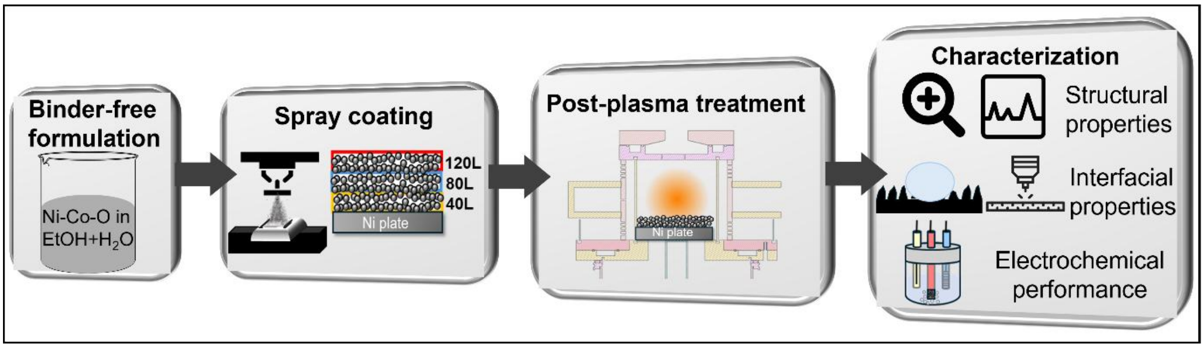

Figure 1. Schematic illustration of the experimental strategy and characterization employed in this study to fabricate binder-free anodes.

2.1 Morphology, surface topography, and porosity evolution

After spray coating and drying, with and without plasma treatment, the morphology of the Ni-Co-O electrodes, both with and without plasma treatment, was examined by scanning electron microscopy (SEM), as shown in **Figure 2**. **Panels a-c** present the as-prepared electrodes (40L, 80L, 120L), while **panels d-f** show the corresponding plasma-treated electrodes (PT-40L, PT-80L, PT-120L). The 40L electrodes show localized substrate exposure, while the 80L and 120L coatings display dense and continuous microstructures. Following plasma treatment, the surface evolves into clustered nanoislands composed of literally coalesced nanoparticles approximately 50-100 nm in diameter. This localized surface reconstruction is in line with the findings of Vinayakumar et al.[24] and hypothesized to be driven by ionized nitrogen species during plasma treatment.

Optical profilometry (**Figure S2**) was employed to quantify the surface coverage and macroscopic roughness of the Ni-Co-O electrodes. The as-prepared samples exhibited surface coverages of 93.3 ±1.3 %, 96.6 ±1.2 %, and 96.8 ±1.7 % for the 40L, 80L, and 120L electrodes, while the corresponding values after plasma treatment were 93.0 ± 1.1 %, 94.3 ± 0.8 %, and 95.4 ± 1.3 %, respectively. The stronger increase in surface coverage from 40L to 80L reflects the progressive filling of uncovered substrate regions, whereas the minimal difference between 80L and 120L confirms that surface continuity is nearly complete beyond a certain deposition threshold.

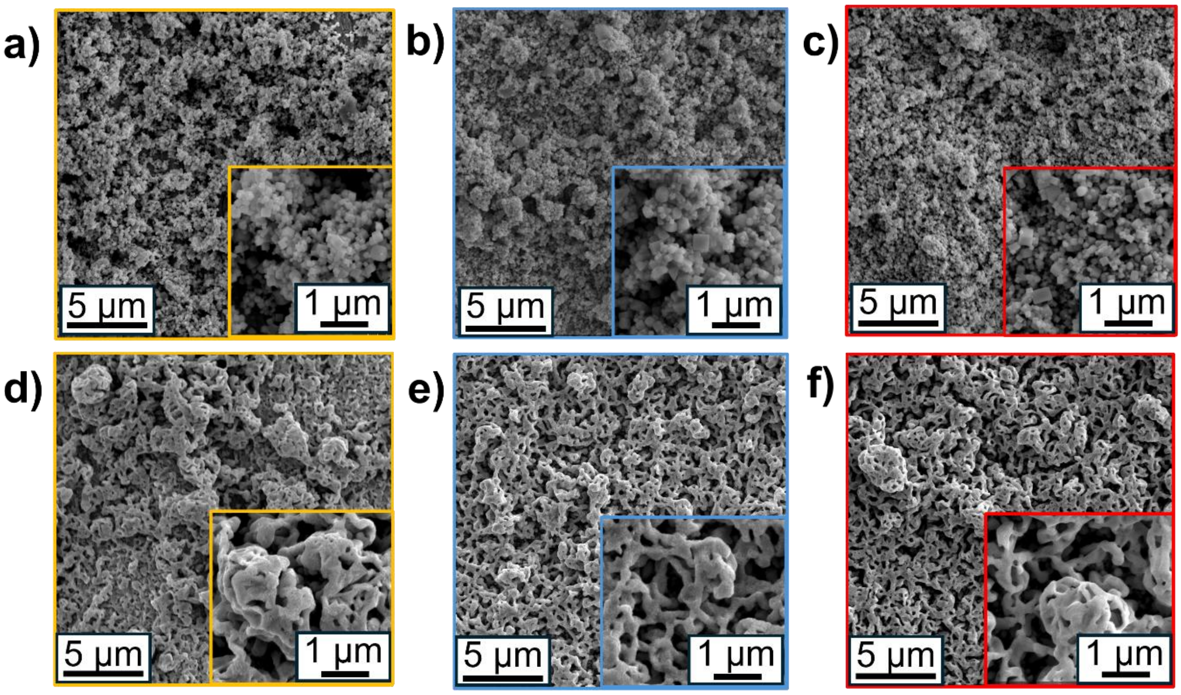

Figure 2. SEM images of Ni-Co-O anodes fabricated via spray coating of the binder-free ink on Ni plate substrates with varying layers: a) 40L, b) 80L, and c) 120L. Corresponding SEM images after plasma treatment are shown in d), e), and f), respectively.

The average macroscopic surface roughness values determined by profilometry were 0.87 µm (40L), 1.47 µm (80L), and 1.65 µm (120L) for the as-prepared electrodes, increasing systematically with the number of deposited layers due to cumulative material buildup and the formation of microscale texture. After plasma treatment, the corresponding roughness values were 0.88 µm (PT-40L), 1.40 µm (PT-80L), and 1.36 µm (PT-120L).

Importantly, the relative roughness trend across thicknesses remains preserved after plasma treatment, with thinner coatings exhibiting lower roughness, and thicker coatings exhibiting higher roughness. However, when comparing each layer individually before and after plasma exposure, the roughness values show only minor variations within the experimental uncertainty, confirming that the applied plasma treatment conditions do not induce large-scale morphological restructuring and instead primarily affect the near-surface region.

Based on the evolution of surface coverage and topography, the electrodes were classified into three distinct regimes. The thin-layer regime (40L and PT-40L) exhibits partial substrate exposure, where incomplete surface coverage with catalyst leaves areas of the Ni support visible. The intermediate regime (80L and PT-80L) achieves nearly full surface coverage, whereas the thick-layer regime (120L and PT-120L) forms continuous, bulk-like films with complete catalyst coverage and minimal exposed substrate areas.

The topographical analysis of the plasma-treated samples was performed using atomic force microscopy (AFM) as shown in **Figure 3a-c**. At this point it has to be mentioned that AFM measurements could not be performed on the as-prepared samples due to their mechanical instability, which led to partial film delamination under the applied tip forces during scanning. This observation already highlights the limited mechanical robustness of the untreated coatings that will be discussed in more detail in Section 2.3.

Multistage data quantification[26] (MSDQ) was used to quantify the surface features of the anodes shown in **Figure S3**. The root-mean-square roughness (Rq) values of the plasma-treated electrodes were 0.45 μm (PT-40L), 0.77 μm (PT-80L), and 1.25 μm (PT-120L), showing a systematic increase with layer number. The lower roughness of PT-40L reflects its comparatively thin architecture, where the plasma treatment affects a substantial fraction of the catalyst layer. In contrast, thicker coatings retain more pronounced nanoscale asperities originating from the cumulative particle stacking during spray deposition. These nanoscale topographical differences are expected to influence electrochemically accessible sites and interfacial electrolyte interaction, effects that are quantitatively evaluated in the electrochemical analysis presented in Section 2.4.

Finally, focused ion beam-scanning electron microscopy (FIB-SEM) cross-sectional imaging was performed to examine the internal microstructure of the plasma-treated electrodes (**Figure 3d-f**). The areal pore fraction, determined from binarized cross-sectional images as the ratio of pore area to total analyzed area (see Experimental Section 4.2.4), was comparable across all plasma-treated samples, indicating that the overall porosity remained largely unchanged with increasing layer number.

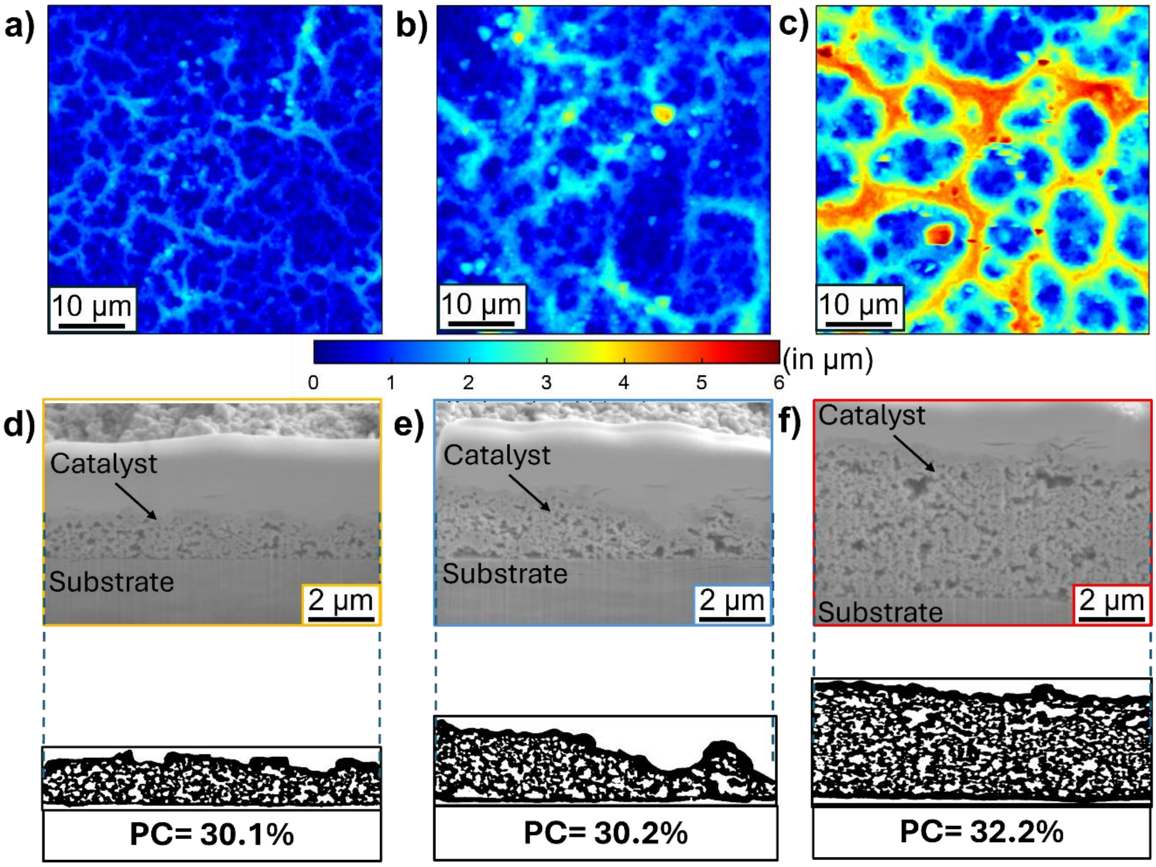

Figure 3. AFM images of Ni-Co-O anodes fabricated via spray coating on Ni plate substrates with varying numbers of deposition layers after PT: a) PT-40L, b) PT-80L, and c) PT-120L. Corresponding FIB-SEM analysis for d) PT-40L, e) PT-80L, and f) PT-120L showing pore coverage (PC) based on binary images.

Despite this similarity in the total pore fraction, clear differences in pore morphology were observed. The PT-40L electrode exhibited a lower pore number density with a relatively narrow pore size distribution. In contrast, the PT-80L and PT-120L samples displayed a higher pore number density and a broader pore size distribution, characterized by more numerous and more uniformly distributed voids throughout the catalyst layer (**Figure S4**). Thus, while the total pore area remains similar (30.1-32.2 %), thicker coatings exhibit a finer and more distributed pore network. As plasma treatment did not significantly alter macroscopic roughness or surface coverage, these structural differences originate primarily from the cumulative stacking and packing behavior during multilayer spray coating rather than from plasma-induced restructuring. The influence of pore architecture on electrolyte accessibility and electrochemical performance is evaluated quantitatively in Section 2.4.

2.2. Surface and bulk characterization

Given that plasma activation is inherently surface-localized, resolving the compositional and chemical gradients within the outermost region of the multilayer coatings is essential. Since the OER is governed by surface redox transitions, modifications occurring within the first few nanometers are expected to disproportionately influence catalytic performance and interfacial properties. Therefore, depth-sensitive characterization techniques were employed to distinguish near-surface reconstruction from bulk composition.

The elemental composition of the Ni-Co-O coatings was examined using XPS to probe the outermost ~5-10 nm of the material. **Figure 4a** presents the XPS-derived atomic fractions of O, Co, and Ni for the investigated samples. For the as-prepared samples, the surface Co content was 45 % (40L), 49 % (80L), and 45 % (120L), whereas after plasma treatment it increased to 56 %, 55 %, and 56 %, respectively. This corresponds to a relative Co enrichment of approximately 10 % at the surface. Concomitantly, the Ni fraction decreased proportionally, indicating plasma-induced compositional redistribution within the near-surface region. In contrast, the O atomic fraction remained essentially unchanged after plasma treatment within experimental uncertainty. This indicates that nitrogen plasma exposure does not significantly modify the O sublattice at the probed depth but instead drives selective redistribution of transition-metal cations. A comparable preservation of the oxide framework during N_2 plasma modification has been reported by Kermanshahi et al.[27], where plasma treatment introduced Ni-N and NH_3 surface species without altering the native NiO structure or overall O signal intensity.

During plasma treatment, the substrate temperature reached approximately 300 °C, as measured by a thermocouple attached to the sample holder. The process was carried out at 1 mbar N_2, conditions that combine elevated temperature with reduced pressure and energetic plasma species. Such environments are known to promote surface segregation phenomena in multicomponent systems rather than bulk phase transformations. Manova et al.[28] demonstrated that plasma-assisted treatments can induce element redistribution and surface enrichment through thermally activated diffusion processes under low-pressure conditions. Similarly, Law et al.[29] reported pressure- and temperature-dependent surface compositional changes in NiCo alloys, showing that elevated temperatures favor preferential Co enrichment at the outermost surface as detected by XPS. N_2 plasmas are furthermore known to generate surface defects, adsorbates, and nitrogen-containing species (e.g., metal nitrides, M–N bonds) that significantly modify the surface chemistry[21,30]. Such defects and reactive species can accelerate near-surface diffusion kinetics and alter the relative stability of Co-rich versus Ni-rich oxide/oxyhydroxide layers, thereby further promoting the formation of a Co-enriched surface layer. In our case, the Co enrichment is confined to the XPS information depth, indicating that the compositional change is limited to the near-surface region. Under the present plasma conditions, the observed increase in the surface Co content is therefore consistent with a plasma-assisted, thermally activated surface segregation process, while transformation of the bulk phase can be excluded based on the absence of compositional changes in the subsurface region.

To further probe electronic states, high-resolution deconvoluted spectra of Ni2p, Co2p, and O1s were analyzed (**Figure S5.1-S5.2**). For the as-prepared samples before plasma exposure, the Ni $2p_{3/2}$ region exhibited distinct components at approximately 854.5 eV (Ni^{2+}) and 856.1 eV (Ni^{3+}), accompanied by characteristic shake-up satellite features (at 861 eV), confirming the existence of both oxidation states. Similarly, the Co $2p_{3/2}$ spectra displayed peaks at approximately 780.0 eV (Co^{2+}) and 781.5 eV (Co^{3+}). The O1s spectra consisted of lattice O (~529.5 eV) and hydroxyl-related species (~531-532 eV), consistent with the formation of a mixed metal oxide.

The plasma-treated samples exhibited similar spectral features, with no additional components or noticeable changes in peak positions. The binding energy variation remained below 0.2 eV. These results indicate that plasma treatment primarily induces compositional redistribution, manifested as Co enrichment at the surface rather than altering the intrinsic oxidation states of Ni and Co, or generating detectable O-vacancy-related spectral features within the XPS probing depth.

To further elucidate the depth-dependent compositional distribution after plasma treatment, XPS depth profiling was performed on representative plasma-treated samples with a sputtering rate of 7 nm min^{-1} (**Figure S6**). Due to the time-intensive and resource-demanding nature of XPS sputter profiling, depth analysis was conducted at a single representative surface location for each electrode. While spatially averaged information is therefore limited, the obtained trends provide clear insight into the vertical composition-gradient induced by plasma exposure.

For PT-40L, the near-surface region (0-5 min etching) exhibits a Co content of approximately 60-62 at%, while Ni is around 32-35 % and O ~5-7 %. With increasing etching time, Co decreases progressively to ~42 at% at 180 min, whereas Ni increases to ~53-55 %, indicating a compositional transition toward the bulk Ni-rich region. A similar trend is observed for PT-

80L. At short etching times, Co is approximately 55-58 %, Ni ~33-36 %, and O ~7-10 %. Upon extended etching (150-180 min), Co decreases to ~45 at% while Ni increases to ~40–42 %. For PT-120L, the surface region shows Co ~52-56 % and Ni ~38–42 %, with O ~6-9 %. After prolonged etching (upto 1.2 µm), Co decreases to ~42-44 %, while Ni increases to ~42-45 %.

In all three samples, the most pronounced compositional changes occur within the initial ~20-30 min of etching, beyond which the elemental fractions approach quasi-stable values. These results confirm that plasma-induced Co enrichment is predominantly confined to the near-surface region, while the bulk stoichiometry remains comparatively stable. The observed gradients therefore support a surface-localized reconstruction mechanism rather than a uniform bulk transformation.

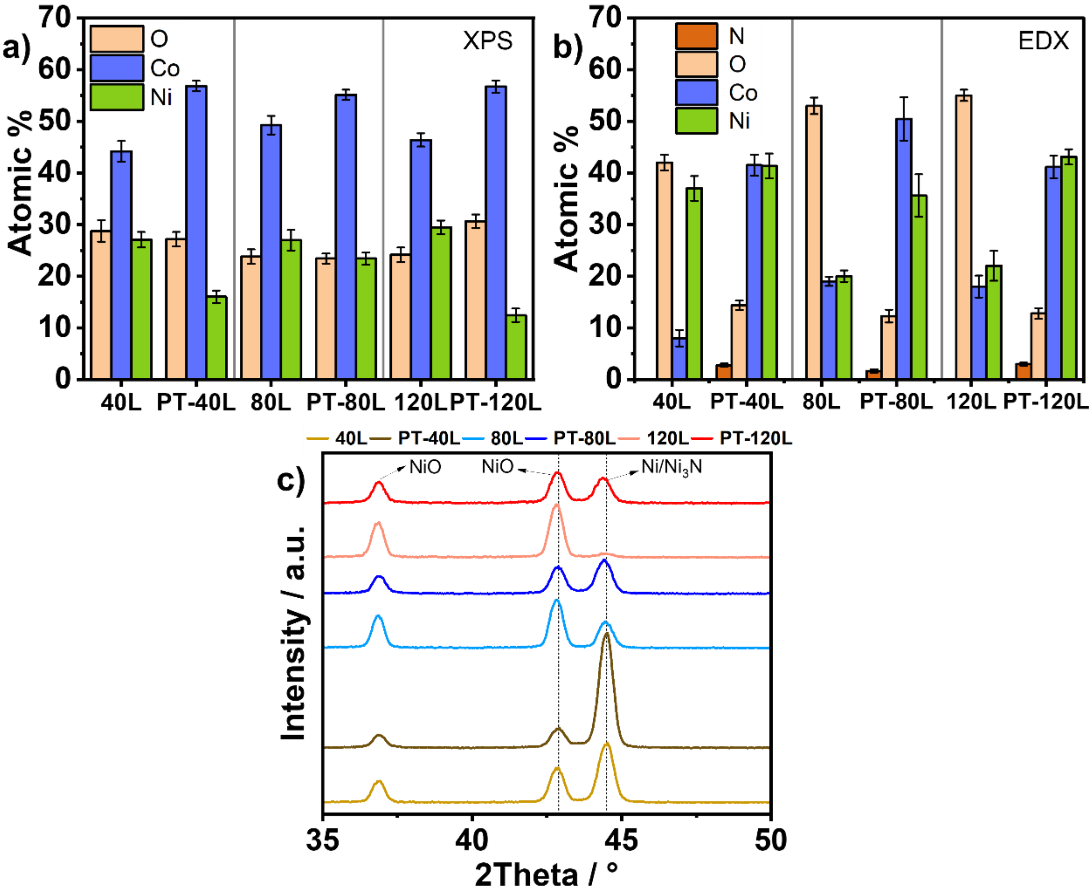

Figure 4. a) Surface elemental composition (from XPS analysis) showing O, Co, and Ni contents for as-prepared and plasma-treated anodes. b) Bulk elemental composition (from EDX analysis) showing O, Co, and Ni contents for as-prepared and plasma-treated anodes (EDX). c) XRD patterns of as-prepared and plasma-treated anodes recorded at a grazing incidence angle of ω = 1.5°, highlighting phase composition and plasma-induced structural changes.

To complement this surface-sensitive, depth-resolved analysis, bulk-averaged elemental composition was subsequently examined using energy-dispersive X-ray spectroscopy (EDX), which probes a significantly larger penetration depth (~ 1 μm). This combined approach enables differentiation between near-surface plasma-induced redistribution and global changes in composition across the full coating thickness. For each electrode, approximately 20 spatially distributed measurement points were collected, and the reported atomic fractions represent averaged values over these locations.

Figure 4b presents the EDX-derived elemental fractions of O, Co, and Ni across the bulk of the Ni-Co-O coatings. For the 40L sample, the Ni content was approximately 35 at%, which increased to ~40 at% in PT-40L. In the 80L and 120L samples, the Ni content was approximately 20 at%, increasing to ~35 at% (PT-80L) and ~40 at% (PT-120L) after plasma treatment. In contrast, the Co content in the as-prepared coatings was approximately 10 at% (40L) and ~20 at% (80L and 120L). After plasma treatment, Co increased substantially to ~40 at% (PT-40L), ~50 at% (PT-80L), and ~40 at% (PT-120L). The O fraction in the as-prepared samples ranged between 40-50 at%, whereas in all plasma-treated samples it decreased to approximately ~10 at%. In addition, N was detected in the plasma-treated electrodes, with an average content of ~3-4 at% across the measurement points, although its presence was not uniform at every location. This indicates heterogeneous nitrogen incorporation within the bulk coating. This depth-dependent distribution suggests diffusion-controlled N incorporation during plasma treatment.

The comparatively high Ni content observed in the 40L electrode can be attributed to partial substrate exposure and the limited coating thickness, allowing the EDX interaction volume to include contributions from the metallic Ni substrate. This substrate contribution becomes less significant in thicker coatings, explaining their lower initial Ni fractions. The substantial increase in the Co content confirms that the Co enrichment observed by surface-sensitive XPS is not restricted to the outermost surface but extends into the bulk of the coating. The substantial decrease in O content after plasma treatment suggests partial depletion of O within the bulk of the coating. Under the applied conditions (~300 °C, reduced-pressure N_2 plasma), O removal can occur via plasma-assisted reduction processes. Energetic nitrogen species and ion bombardment are known to promote O desorption from transition-metal oxides under low-pressure environments, particularly at elevated temperatures, leading to subsurface O deficiency[28,31]. The differences between XPS and EDX results originate from their distinct information depths. While XPS probes only the outermost ~5-10 nm and therefore captures surface-specific compositional changes, EDX averages over a substantially larger interaction volume extending deeper into the catalyst layer. Consequently, XPS reveals stronger surface Co enrichment and Ni depletion, whereas EDX reflects the average composition of the modified and unmodified regions. Together with the depth-profile XPS measurements, these results indicate that plasma treatment generates a depth-dependent compositional gradient rather than a uniform modification throughout the entire coating.

Furthermore, because the XPS measurements were performed after exposure to air, reoxidation of the outer surface is expected. As a result, the surface-sensitive XPS spectra primarily reflect the reoxidized surface layer, whereas EDX remains sensitive to oxygen depletion within the subsurface region. The combined XPS and EDX analyses therefore suggest that oxygen loss occurs predominantly beneath the outermost reoxidized surface during plasma treatment.

To complement the surface-sensitive XPS and bulk-averaged EDX analyses, grazing-incidence X-ray diffraction (GIXRD) was employed to elucidate the crystallographic structure and phase composition of the Ni-Co-O coatings. The measurements were conducted at an incidence angle of $\omega = 1.5°$, corresponding to an estimated X-ray penetration depth of approximately 100-200 nm, depending on material density and absorption coefficient. This configuration enhances near-surface sensitivity while minimizing substrate contribution, thereby enabling assessment of structural modifications within the upper region of the coating.

Figure 4c presents the GIXRD patterns of the as-prepared and plasma-treated electrodes. The Bragg reflections observed at 2Theta positions of approximately 37.2°, 43.3°, and 44.5° are consistent with mixed Ni-Co-O phases together with contributions from metallic Ni, likely originating from the underlying substrate and/or Ni-rich domains within the coating[32]. The reflections near 37.2° and 43.3° correspond to characteristic planes of NiO/CoO-type structures, and the peak at ~44.5° is primarily associated with the (111) reflection of face-centered cubic (fcc) metallic Ni phase[24,33]. After plasma treatment, the overall diffraction framework remains largely preserved, indicating that the dominant crystalline oxide structure is maintained. However, a noticeable enhancement of the reflection at approximately 44.5° is observed across all thicknesses. This diffraction angle coincides with the (111) plane of hexagonal Ni_3N (PDF#10-0280), which has been reported at ~44.5° together with additional reflections at 38.6°, 42.1°, 58.5°, 70.6°, and 78.4° in Ni_3N-containing systems[34]. While the peak at 44.5° also overlaps with the (111) reflection of metallic Ni, the systematic intensity increase after plasma treatment, combined with measurable bulk nitrogen incorporation (3-4 at% by EDX), suggests that partial subsurface nitridation of Ni-rich domains may contribute to this enhancement. This enhancement is attributed to the formation of a Ni_3N phase at the surface. Ni_3N is a plasma-induced byproduct that likely arises from the interaction between activated species in the nitrogen plasma and Ni sites, leading to partial nitridation[23]. After formation, it is incorporated in the material upon structural reorganization[35]. Importantly, no distinct additional Ni_3N-specific peaks are clearly resolved, indicating that any nitride formation is likely limited, highly dispersed, or confined to the subsurface region rather than forming a dominant bulk phase. This interpretation is consistent with the XPS results, which show <1 at% nitrogen at the outermost surface, supporting a depth-dependent nitrogen distribution rather than uniform surface nitride formation.

When considered together with the XPS and EDX results, the GIXRD data indicate that N_2 plasma treatment primarily induces compositional redistribution and depth-dependent chemical modification rather than a fundamental alteration of the crystalline phase composition. XPS reveals enrichment of surface Co without detectable nitrogen incorporation at the outermost ~10 nm, whereas EDX indicates subsurface nitrogen incorporation and O depletion within the bulk. The preservation of the dominant diffraction framework confirms that plasma treatment selectively modifies near-surface and subsurface chemistry while maintaining the structural backbone of the multilayer Ni-Co-O electrodes. These plasma-induced chemical and structural modifications are expected to directly influence surface energy and interfacial interactions, which are examined in the following section through wettability and adhesion analysis.

2.3. Wettability and plasma-induced mechanical reinforcement

2.3.1 Wetting analysis

To assess the wetting behavior of the coatings, contact angle measurements were conducted with 1 M KOH. For both the as-prepared and plasma-treated layers, the droplet spreading followed a Wenzel-type wetting behavior[36], indicating that surface roughness amplifies the intrinsic wettability of the material. To quantitatively compare the lyophilicity of the anodes, the temporal evolution of the contact angle was analyzed until the droplet was fully spread[37]. As shown in **Figure 5a**, among the as-prepared electrodes, both 40L and 80L required approximately 11 s to reach ~15°, whereas the 120L sample exhibited the fastest spreading (3 s) to reach the same angle. Thus, the ranking of wetting kinetics was 120L > 40L ≈ 80L, with the thickest coating enabling nearly four times faster droplet spreading compared to the thinner counterparts. After plasma treatment (**Figure 5b**), droplet spreading was dramatically accelerated for all samples. The time required to reach ~15° decreased to approximately 0.3 s for PT-40L, 1 s for PT-80L, and 0.1 s for PT-120L. The relative ranking remained consistent (PT-120L > PT-40L > PT-80L), while the absolute spreading times decreased by more than an order of magnitude compared to the untreated electrodes.

The comparable spreading times observed for 40L and 80L in the as-prepared state indicate that substrate exposure and coating morphology exert competing effects. The partially exposed Ni substrate in 40L, which is intrinsically lyophilic in alkaline media[38], contributes to rapid wetting. In contrast, the 80L sample suppresses the beneficial substrate influence but does not yet exhibit the enhanced roughness of 120L, resulting in similar overall spreading kinetics like 40L.

The superior wetting performance of the 120L electrode in both series correlates with its continuous catalyst coverage and higher macroscopic roughness, as established by optical profilometry analysis. Under Wenzel wetting conditions, where liquid penetrates into the surface pores, increased roughness enhances the effective solid-liquid contact area and facilitates capillary-driven infiltration, thereby accelerating droplet spreading.

After plasma treatment, the pronounced acceleration in droplet spreading is attributed primarily to surface chemical modification rather than large-scale morphological restructuring. Optical profilometry revealed a negligible change in the macroscopic roughness after plasma treatment, although AFM analysis showed nanoscale restructuring characterized by granular feature formation. Since droplet spreading occurs over millimeters, macroscopic roughness and surface chemistry dominate wetting kinetics, while nanoscale rearrangements contribute secondarily by increasing the effective surface area.

XPS analysis confirmed that all plasma-treated samples exhibit increased surface Co content compared to their as-prepared counterparts. While the magnitude of Co enrichment is similar among the plasma-treated samples and therefore does not explain the relative ranking, the overall compositional shift contributes to enhanced intrinsic surface affinity toward the alkaline electrolyte. Co-rich oxide surfaces are known to exhibit strong hydroxyl adsorption tendencies in alkaline environments[39,40], which can increase solid-liquid interaction and reduce the apparent contact angle. Additionally, subsurface nitrogen incorporation detected by EDX, together with Ni_3N formation observed by GIXRD may modify local electronic structure and surface energy, further contributing to improved wettability.

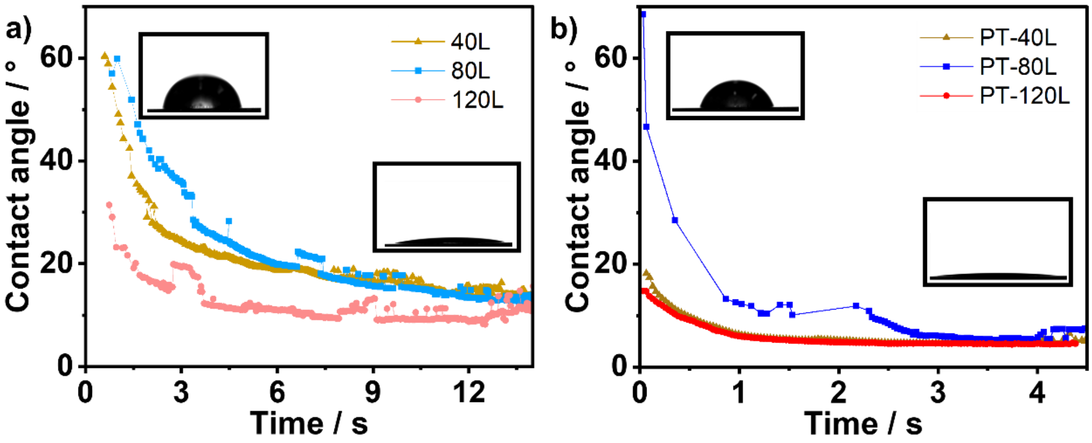

Figure 5. Time-resolved contact angle measured placing a 1 M KOH droplet on a) as-prepared electrodes and b) plasma-treated electrodes, illustrating the dynamic wetting behavior of the anode surfaces. Note that the time axis scaling differs between a) and b) to account for the substantially faster spreading kinetics observed after plasma treatment.

Taken together, the results indicate that plasma treatment enhances intrinsic surface energy across all samples, while thickness-dependent micro-roughness and pore architecture govern the relative wetting hierarchy. The accelerated spreading kinetics therefore arise from a synergistic effect of plasma-induced surface chemical modification and morphology-controlled amplification of the wetting by the Wenzel state.

2.3.2 Mechanical stability

To assess structural integrity of these electrodes, mechanical adhesion strength, a critical factor for ensuring long-term electrode stability in AWE, was quantitatively assessed using shear testing (details are provided in the Experimental Section 4.3.2). The corresponding failure modes and measured adhesion strengths are summarized in Figure 6.

All as-prepared samples exhibited adhesive interfacial failure, characterized by complete detachment of the catalyst layer from the Ni substrate (**Figure 6a**). The fracture surface revealed clean delamination at the coating-substrate interface, indicating weak interfacial bonding in the absence of plasma treatment. This observation is consistent with the mechanical instability noted during AFM measurements (Section 2.1), where untreated films showed poor mechanical robustness under tip interaction. This poor mechanical stability precludes further electrochemical processing, as delamination during OER testing would compromise both performance and reliability.

In contrast to the untreated electrodes, the plasma-treated anodes exhibited markedly improved mechanical integrity. The PT-40L electrode showed no observable failure under the applied shear load (**Figure 6b**), indicating that its adhesion strength exceeded the measurable range of the test configuration. In comparison, PT-80L and PT-120L exhibited cohesive failure within the catalyst layer (**Figure 6c-d**), with residual material remaining on both the Ni substrate and the loading fixture. This transition from interfacial failure in untreated films to cohesive or no failure after plasma treatment confirms substantial strengthening of the coating–substrate interface.

The measured shear strengths increased significantly following plasma treatment. PT-40L exhibited the highest apparent adhesion strength (2.1 ± 0.5 MPa), followed by PT-80L (1.5 ± 0.3 MPa) and PT-120L (1.3 ± 0.3 MPa). The superior adhesion of PT-40L is attributed to a more effective plasma activation throughout the thinner coating, allowing ionized species to reach and modify the coating-substrate interface directly. Plasma exposure at elevated temperature (~300 °C) likely enhances interfacial bonding through surface activation of the Ni substrate, strengthening of metal-oxygen (M-O) interfacial linkages, and nanoscale restructuring that increases the effective contact area.

As the coating thickness increases (80L and 120L), the relative penetration depth becomes smaller compared to the total film thickness. Consequently, although the interface remains significantly strengthened compared to untreated samples, internal cohesive fracture becomes the dominant failure mode in thicker films. The moderate decline in the measured shear strength with increasing thickness is therefore attributed to reduced interfacial activation combined with higher internal stress within thicker multilayer coatings. Together, these findings demonstrate that plasma treatment enhances both wettability and adhesion, two indispensable attributes for stable and efficient anode operation in AWE.

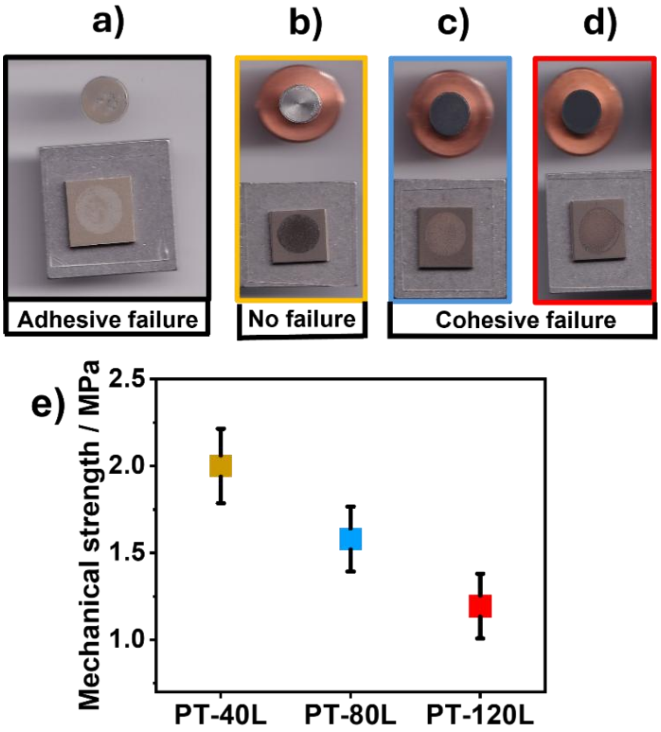

Figure 6. Images after adhesion testing for the a) as-prepared sample, b) PT-40L, c) PT-80L, and d) PT-120L. e) Mechanical strength at failure of all plasma-treated samples.

Building upon the demonstrated improvements in interfacial wettability and mechanical robustness induced by plasma treatment on the level of anode layer properties, the following section investigates the electrochemical implications of these modifications. Complementary operando Raman spectroscopy is employed to directly probe the potential-dependent structural and chemical evolution of the Ni-Co-O anodes under OER conditions.

2.4 Electrochemical analysis

2.4.1 Operando Raman measurements

The operando Raman spectra were evaluated as difference plots referenced to 1.55 V vs. RHE, a potential within the OER regime where the electrode surface is expected to be in a highly oxidized state. This reference was chosen to establish a stable oxidized baseline, enabling clear identification of structural changes occurring upon stepping to lower potentials (experimental details provided in Section 4.4.1). Because the spectra are referenced to 1.55 V, the difference plots highlight structural evolution occurring during reduction from the oxidized state, rather than oxidation toward it. To verify structural reversibility, Raman spectra collected during anodic and cathodic sweeps are provided in **Figure S8**. The nearly overlapping responses confirm that the observed transformations are largely reversible under the applied potential window, although minor deviations may arise from contributions of less electrochemically active subsurface regions in thicker films.

Across the plasma-treated multilayer electrodes (PT-40L, PT-80L, and PT-120L), three dominant vibrational features were observed in the operando spectra (**Figure 7a-c**). The band centered at approximately 455 cm^{-1} corresponds to M–O lattice vibrations within the Ni-Co-O framework and remains relatively invariant with the applied potential, serving as an internal structural reference. Given the substantial thickness of the multilayer coatings, contributions from Ni^{2+} and Co^{2+} containing backbone species cannot be excluded, particularly from subsurface regions that may not undergo complete potential-dependent oxidation. In contrast, the bands near 533 cm^{-1} and 611 cm^{-1} exhibit a pronounced potential dependence. Since the spectra are referenced to 1.55 V, a reduction in their intensity upon stepping to lower potentials reflects the reversible transformation of oxidized CoOOH-type species formed at high potential back to lower-valent Co hydroxide or oxide states. The feature at ~533 cm^{-1} is commonly associated with CoOOH-related vibrations in alkaline media, whereas the weaker band at ~611 cm^{-1} is attributed to highly oxidized CoOOH-like species or distorted Co-O environments. Although less intense than the 533 cm^{-1} band, its potential-dependent evolution follows the same trend, supporting its assignment to oxidized cobalt surface species formed under OER conditions. The decrease of both bands upon cathodic stepping confirms that the electrode surface undergoes reversible redox transitions between oxidized CoOOH-like states at 1.55 V and reduced Co species at lower potentials.

The magnitude of this reversible spectral evolution increases with coating thickness. PT-40L exhibits the smallest modulation of the 533 and 611 cm^{-1} features, whereas PT-120L shows the most pronounced intensity variation. Quantitative analysis of peak intensity ratios further supports this observation. The 533/455 ratio, representing the relative abundance of oxidized Co species at 1.55 V, increases progressively from PT-40L to PT-80L and PT-120L, indicating that thicker coatings stabilize a higher density of oxidized CoOOH-type surface species under anodic polarization. In contrast, the 611/455 ratio also increases with thickness but approaches a plateau between PT-80L and PT-120L. This saturation behavior suggests that formation of the highly oxidized Co environment is surface-limited. Considering that Raman excitation at 532 nm can probe several nanometers into the catalyst layer, particularly in thicker films, the observed plateau may reflect a combination of surface-limited oxidation and subsurface contributions from less oxidized bulk regions. Thus, although multilayer deposition enhances the overall density of redox-active Co species, the most highly oxidized states appear constrained by surface accessibility.

In addition to Co-related features, Ni-Co-O systems typically exhibit NiOOH-associated bands near approximately 480 cm^{-1} and 550 cm^{-1}. In the present spectra, these Ni-related contributions overlap with Co-derived modes and do not show pronounced independent modulation in the difference plots. This indicates that the dominant potential-dependent structural evolution detected under operando conditions arises primarily from Co-centered redox transitions within the mixed-metal oxyhydroxide framework, while Ni species likely participate in the overall redox process without producing separately resolved spectral signatures under the applied measurement conditions.

Mechanistically, the observed variation in the near-surface Ni and Co composition is attributed to plasma-induced cation redistribution within the outermost surface region (refer to Section 2.2). In contrast to bulk diffusion processes, this redistribution originates from non-equilibrium surface activation induced by energetic plasma species, which generate oxygen vacancies, defect sites, and localized transient heating. These effects collectively enhance cation mobility and can promote kinetically driven elemental segregation in mixed transition-metal oxides[29].

Such plasma-assisted defect engineering has been previously reported to induce pronounced surface reconstruction in multicomponent oxide systems, often accompanied by changes in local electronic structure and catalytic activity. In particular, recent studies have shown that defect- and vacancy-rich surfaces can facilitate dynamic formation of (oxy)hydroxide phases under anodic potentials, which are widely recognized as the active phase in alkaline oxygen evolution catalysis[41,42].

In the present work, the Co enrichment detected by XPS, together with the enhanced CoOOH-related Raman signatures under operando conditions, indicates that plasma treatment promotes preferential stabilization of Co-rich surface domains. These domains likely act as precursors for the electrochemically active oxyhydroxide phase, while the bulk Ni–Co oxide framework remains largely preserved.

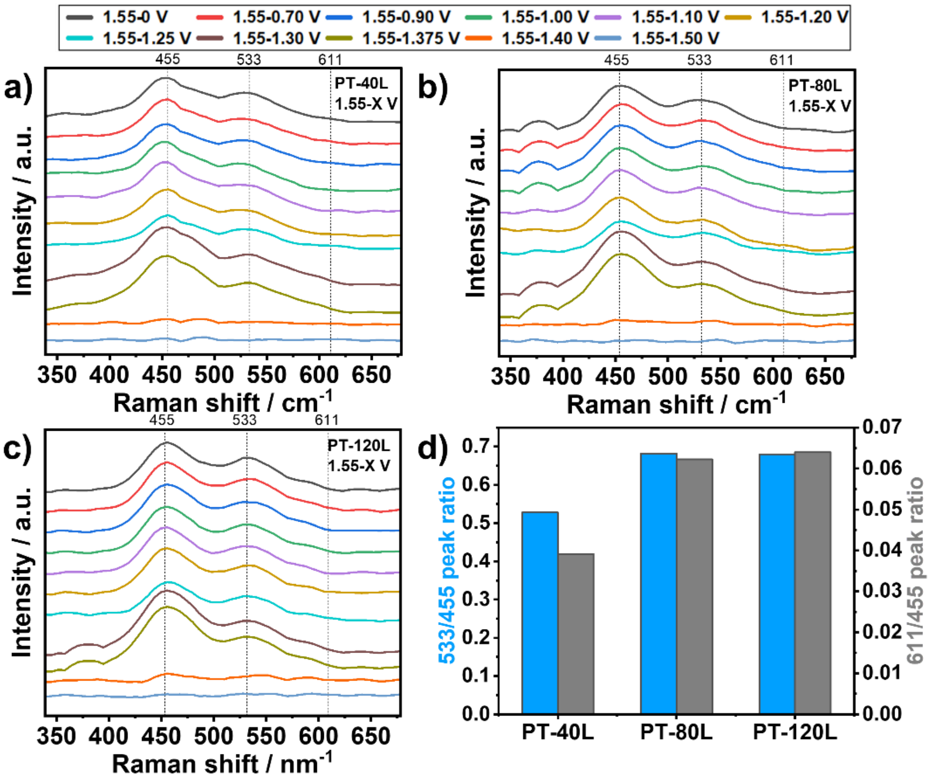

Figure 7. Operando Raman spectra of a) PT-40L, b) PT-80L, and c) PT-120L recorded in 1 M KOH during potential sweeps from 0 V to 1.55 V vs. RHE. The spectra are presented as difference plots relative to the signal at 1.55 V vs. RHE. d) Peak intensity ratios 533/455 and 611/455, associated with Co species, for the plasma-treated samples.

Overall, the operando Raman results demonstrate reversible, potential-dependent structural transitions between reduced oxide states and oxidized CoOOH-type species in plasma-treated multilayer electrodes. The extent of these transformations increases with coating thickness, indicating that the multilayer architecture influences the density of electrochemically addressable Co sites. At this stage, the Raman data establishes a structural correlation between coating thickness and the extent of Co redox activity. The implications of these transformations for electrocatalytic performance are evaluated in the subsequent electrochemical analysis.

2.4.2 Electrochemical OER measurements in beaker cell

The electrochemical analysis was carried out using a three-electrode beaker cell setup with plasma-treated Ni-Co-O anodes as working electrodes, and with 99.2% pure Ni (denoted Ni99.2) as a reference substrate for comparison. The cyclic voltammetry (CV) conditioning profiles (shown in **Figure S9a**) of plasma-treated anodes were recorded over 50 consecutive cycles to examine the evolution of their redox-active Ni and Co species. All plasma-treated electrodes exhibited broad redox features in the range of 1.30-1.45 V vs. RHE, corresponding to overlapping Ni^{2+}→Ni^{3+} and Co^{2+}→Co^{3+} transitions. Separate Ni and Co peaks were not distinctly resolved due to the peak overlap typical of mixed Ni-Co oxyhydroxide systems[43,44]. Nevertheless, the integrated redox response from the 50th cycle (last cycle) was used to approximate the accessible Ni/Co redox sites[45,46] (**Figure S9b**). PT-40L showed a transferred charge of 1.71 C, PT-80L exhibited 3.73 C, and PT-120L reached 13.1 C. This trend correlates with the increasing nanoscale roughness observed in AFM analysis and the higher pore density revealed by FIB-SEM imaging, indicating improved accessibility of catalytic sites in thicker films.

Electrochemical impedance spectroscopy measurements (**Figure S9c**) showed high-frequency intercept values of 0.50 Ω for PT-40L, 0.74 Ω for PT-80L, and 0.75 Ω for PT-120L. The slightly lower resistance observed for PT-40L is attributed to the partial exposure of the metallic Ni substrate and thinner coating. However, since the differences are minor, variations in catalytic performance are not governed by contact resistance but rather by interfacial and surface-related properties.

The CV analysis (shown in **Figure 8a**) at lower scan rate further demonstrated thickness-dependent OER activity. The potential required to reach 10 mA cm^{-2} was 1.562 ± 0.001 V vs. RHE for Ni99.2, 1.554 ± 0.006 V for PT-40L, 1.532 ± 0.002 V for PT-80L, and 1.511 ± 0.006 V for PT-120L. At 100 mA cm^{-2}, the trend becomes even more clear, with potentials of 1.611 ± 0.003 V for Ni99.2, 1.604 ± 0.012 V for PT-40L, 1.584 ± 0.004 V for PT-80L, and 1.560 ± 0.008 V for PT-120L. Thus, the OER performance improves progressively with increasing layer thickness, with PT-120L exhibiting the lowest potential at both benchmark current densities.

To further evaluate the reaction kinetics, Tafel slopes were extracted from the polarization curves and are presented in **Figure S9d**. For the final cycle shown in **Figure 8a**, PT-40L exhibited a Tafel slope of 49.74 mV dec^{-1}, PT-80L showed 42.32 mV dec^{-1}, and PT-120L displayed the lowest value of 40.06 mV dec^{-1}. The progressive decrease in Tafel slope with increasing coating thickness indicates increasingly favorable OER kinetics, consistent with the lower overpotentials observed for the thicker plasma-treated electrodes.

The high activity of PT-120L reflects the combined influence of accessible surface sites, surface micro-roughness, pore density, and plasma-induced Ni/Co compositional redistribution[47]. As demonstrated by XPS, plasma treatment enriches Co at the near-surface region while redistributing Ni species. Since CoOOH-type surface species are widely recognized as highly active phases for alkaline OER, this Co enrichment contributes directly to improved intrinsic catalytic activity[48,49]. Operando Raman spectroscopy showed that thicker plasma-treated coatings stabilize a larger population of oxidized CoOOH-type species under anodic polarization, while XPS and EDX analyses confirmed compositional redistribution at the surface and the near-surface region. The larger transferred charge in PT-120L, together with enhanced roughness and structural development, indicates more efficient utilization of redox-active sites during OER. Simultaneously, improved wettability (spreading time reduced from 3 s to 0.1 s after plasma treatment) promotes rapid electrolyte infiltration and minimizes interfacial contact resistance between the catalyst layer and electrolyte. Enhanced mechanical adhesion further stabilizes the catalyst-substrate interface, reducing the likelihood of interfacial delamination and preserving electronic contact between the catalyst layer and the metallic Ni support during operation.

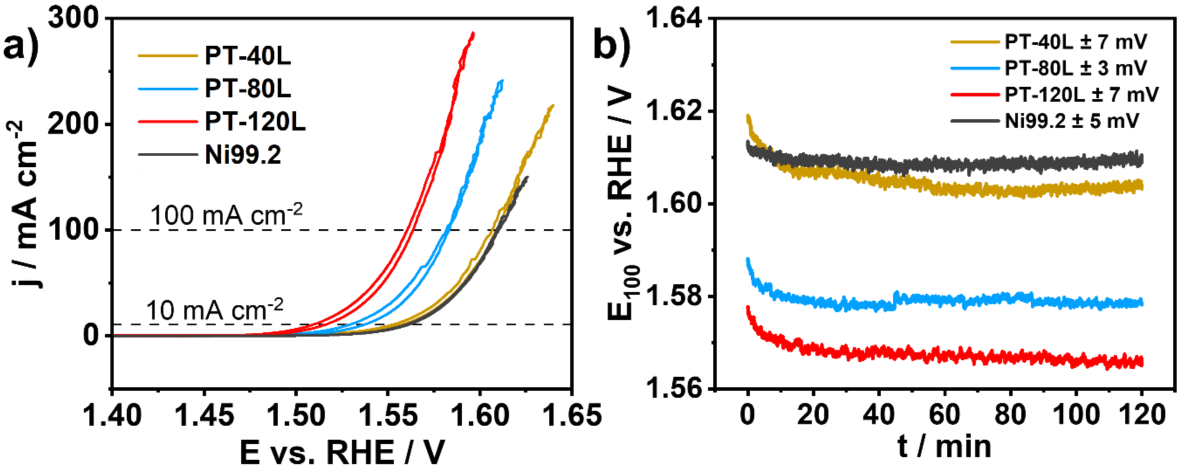

Figure 8. a) CVs for plasma-treated samples PT-40L, PT-80L, PT-120L, and the bare Ni99.2 substrate as reference. b) CP measurements for the final stability sequence (see experimental details) at 100 mA cm^{-2} of the spray coated plasma-treated samples PT-40L, PT-80L, PT-120L, and the bare Ni99.2 substrate. All measurements performed in 1 M KOH at room temperature (RT).

Figure 8b shows the steady-state chronopotentiometry (CP) analysis for the final 120 min segment of the 480 min protocol at 100 mA cm^{-2} that demonstrates stable operation for all plasma-treated electrodes (details in Experimental Section 4.4.2). The complete 8 h dataset is provided in **Figure S9e**. The Ni99.2 electrode stabilized at approximately 1.61 V vs. RHE, PT-40L stabilized at ~1.60 V, PT-80L at ~1.58 V, and PT-120L at ~1.57 V. An initial decrease in potential was observed for all plasma-treated electrodes prior to stabilization, consistent with progressive surface reorganization and activation under alkaline OER conditions. No visible catalyst delamination was observed during the CP testing, in agreement with the enhanced adhesion strength measured in mechanical stability testing.

The superior performance of PT-120L arises from the synergistic interplay between enhanced nanoscale roughness, greater pore density, plasma-induced Ni/Co compositional redistribution, markedly improved wettability, and strengthened interfacial adhesion. While PT-80L exhibits the highest conditioning-induced redox activation, optimal steady-state OER activity is achieved only when the formation of redox-active species is coupled with sufficient morphological accessibility and structural integrity that enable efficient utilization of those active sites under steady-state operation.

Collectively, these findings demonstrate that steady-state OER performance in multilayer Ni-Co-O electrodes is not governed solely by electrochemical activation, but by the integrated coupling of surface roughness, surface chemistry, multiscale surface morphology, electrolyte accessibility, and interfacial robustness (**Figure 9**). This work highlights the importance of simultaneously engineering chemical composition, electrode architecture, and interface stability to unlock the full catalytic potential of plasma-modified multilayer oxide systems for AWE.

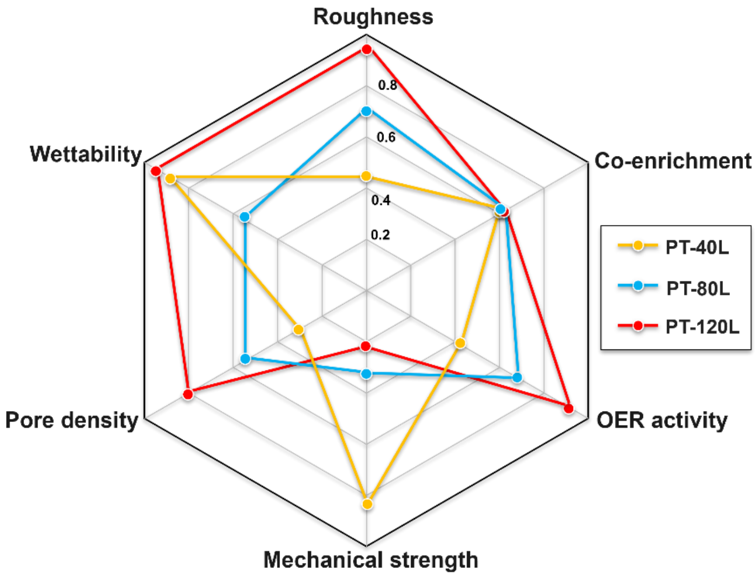

Figure 9. Radar chart representing different factors for the three spray-coated plasma-treated anodes.

To further contextualize the electrochemical performance of the binder-free plasma-treated anodes, Table 2 summarizes the overpotentials of the PT-40L, Pt-80L, and PT-120L anodes investigated in this study and compares them with representative binder-free Ni-Co-O-based anodes reported in the literature. This comparison is intended to situate the present results within the broader field and to highlight the methodological contribution of this study.

Table 2. Comparison of electrochemical performance and processing characteristics of binder-free Ni-Co-O anodes prepared via plasma treatment in this study, alongside representative binder-free Ni-Co-based anodes reported in the literature. Overpotentials are reported at geometric current densities of 10 and 100 mA cm^{-2} in alkaline electrolyte. The comparison is intended to contextualize the present results and highlight differences in fabrication strategy and scalability rather than to benchmark intrinsic catalytic activity. Literature values are reported as provided in the respective references; differences in electrode architecture, electrolyte composition, and testing protocols may affect direct comparability.

Material	**Processing technique**	**Overpotential @10 mA cm^{-2}**	**Overpotential @100 mA cm^{-2}**	**Key advantage**	**Key limitation**
PT-40L (Ni-Co-O)	Binder-free (Spray coating + Plasma)	324 mV	374 mV	Excellent adhesion	Lower active surface development
PT-80L (Ni-Co-O)	Binder-free (Spray coating + Plasma)	302 mV	354 mV	Balanced morphology	Moderate adhesion reduction
PT-120L (Ni-Co-O)	Binder-free (Spray coating + Plasma)	281 mV	335 mV	Highest surface roughness, wettability, and Co active species	Further thickness increase may reduce mechanical robustness
$NiCoP@Cu_3P/CF$[50]	Direct oxidation of Cu Foam	309 mV	-	Excellent catalytic activity due to synergistic bimetallic phosphide interfaces and hierarchical morphology	Complex multi-step synthesis; performance strongly dependent on Cu foam architecture

Ni-Fe-Co nanocone[51]	Electro-deposition in a metal chlorides mixture	316 mV	375 mV	Low-cost, scalable electrode fabrication with good electrical connectivity	Precise composition and morphology control can be challenging over large areas
NiO nanorods[52]	Hydrothermal growth on metal substrate	-	350 mV	High surface area and direct electrical contact	Substrate-dependent growth; limited scalability
Ni_3Se_2/Cu Foam[53]	Electro-depostion from a bath of $Ni(OCOCH_3)_2.4H_2O$, SeO_2, LiCl	340 mV (at 50 mA cm^{-2})	-	High intrinsic conductivity and bifunctional HER/OER activity	Se-containing materials raise long-term stability and scalability concerns
NiCo and NiFe on Cu Foams[54]	Electro-deposition, in a bath of Ni, Co, Fe salts	290 mV	410 mV	High porosity, large active surface area, rapid fabrication	Mechanical integrity and uniformity of porous structures may become challenging for scalability

Increasing catalyst loading improves the amount of active material but is accompanied by reduced mechanical stability and limited plasma penetration depth. As plasma modification is primarily restricted to the near-surface region, excessively thick coatings could likely result in a larger inactive fraction of the catalyst layer. Therefore, electrode performance is governed by a trade-off between loading, plasma accessibility, transport, and mechanical integrity.

While the present work demonstrates the benefits of plasma treatment for multi-layer coatings on planar nickel substrates and enables the fabrication of binder-free anodes, evaluation at industrially relevant current densities (1 A cm^{-2}) and extended stability testing represent the next steps. Achieving these conditions requires transitioning from planar substrates to expanded Ni mesh, which is beyond the scope of the current study but defines a clear direction for future research.

3. Conclusion

This work demonstrates that nitrogen plasma treatment provides an effective strategy for stabilizing and activating multilayer Ni-Co-O electrodes through depth-limited surface modification. Plasma exposure induces near-surface compositional redistribution (as confirmed by XPS depth profiling) with Co enrichment and subsurface nitrogen incorporation while preserving the overall crystalline framework. At the same time, interfacial adhesion is markedly strengthened, transforming unstable, delamination-prone coatings into mechanically robust multilayer architectures suitable for electrochemical operation.

Operando Raman spectroscopy reveals reversible redox transitions involving oxidized Co species under OER-relevant potentials, with thicker coatings stabilizing a greater number of electrochemically accessible active sites. Although intermediate thickness (PT-80L) exhibits the strongest conditioning-induced redox activation, the highest steady-state activity is achieved for PT-120L, which delivers an overpotential of 335 mV at 100 mA cm^{-2} (1.565 V vs. RHE) and stable operation under sustained current.

The results collectively show that catalytic performance in multilayer Ni-Co-O systems is governed not simply by electrochemical activation, but by the coordinated optimization of surface composition, structural accessibility, and interfacial stability. By coupling thickness-controlled multilayer design with plasma-driven surface engineering, this study establishes a scalable pathway and design parameters for enhancing catalyst utilization and operational robustness in AWE.

4. Experimental Section

4.1 Anode fabrication and plasma treatment

The catalyst ink was formulated by sequentially dispersing the catalyst material, Ni-Co-O, in a binary solvent system composed of deionized water (Milli Q, 18.2 MΩ cm) and EtOH (VWR International, 99.97 %) in a 1:1 volumetric ratio. To ensure homogeneity and optimal dispersion of the active material, the resulting suspension was subjected to ultrasonic probe sonication using a Hielscher UP200Ht sonicator (Hielscher Ultrasonics GmbH, Germany).

The sonication process was performed under pulse mode for a total duration of 18 minutes. The detailed characterization of the material can be found in our previous study[24].

Ink characterization was performed by utilizing an analytical centrifuge (LUMisizer 6514–44, LUM GmbH). Samples of 410 μL were filled into polycarbonate cells (used for polar protic solvents) and placed inside the centrifuge. All measurements were conducted at 2500 RPM and 20 °C. The captured fingerprints were visualized by transmittograms that enable improved understanding of the sedimentation dynamics and direct comparison of dispersions and inks[55].

Ni (HMW Hauner, 99.2 %, geometric area of 1 cm^2) plates served as the conductive substrate for the fabrication of anodes. Prior to catalyst deposition, the substrates were chemically etched in 1 M HCl for 5 min, followed by sequential cleaning in acetone and isopropanol for 5 min each using an ultrasonic bath (Elmasonic S 30 H, Germany) at RT. The prepared catalyst ink was then supplied to an automated ultrasonic spray-coating system (Sono-Tek Corporation, USA) through a precision-controlled liquid delivery unit[14,24,33].

The catalyst ink was atomized and deposited onto preheated Ni substrates (150 °C) at a controlled flow rate of 0.4 mL min^{-1}. A nozzle-to-substrate distance of 7 cm was maintained throughout the process. To promote uniform film formation, multiple successive spray layers were applied using an alternating deposition scheme. The initial layer was deposited unidirectionally across the substrate surface, while each subsequent layer was applied after rotating the spray direction by 90°, thereby generating an orthogonal cross-hatched architecture. This sequence was repeated until the target number of layers was achieved.

To achieve electrodes with varying catalyst loadings, the number of spray passes was systematically adjusted to yield three distinct sets of samples: 40, 80, and 120 spray layers. The corresponding nominal catalyst loadings were approximately 200 ± 21 μg cm^{-2} (40L), 400 ± 23 μg cm^{-2} (80L), and 600 ± 28 μg cm^{-2} (120L).

Following catalyst deposition, the electrodes were subjected to a post-treatment step using a nitrogen-based microwave plasma to enhance surface wettability and improve electrochemical performance. The treatment was conducted in a custom-built plasma reactor based on a 2.45 GHz IPLAS CYRANNUS I-6" resonator, designed for high process flexibility and potential industrial scalability. The spray coated Ni-Co-O on Ni substrates were placed on a glass holder inside the chamber, which was initially evacuated to remove contaminants. Nitrogen gas was then introduced at a flow rate of approximately 400 sccm, and the system pressure was stabilized at 1 mbar using continuous vacuum pumping. Plasma was ignited by applying 1 kW of microwave power, and E-H tuners were used to minimize reflected power and ensure stable plasma operation. The electrodes were exposed to the nitrogen plasma for 10 minutes under these conditions. After treatment, the plasma and gas flows were terminated, the chamber was re-evacuated to remove residual gases, and the samples were retrieved following venting[23]. The plasma-treated electrodes are denoted as PT-40L, PT-80L, and PT-120L, corresponding to their respective spray-deposited layer counts.

4.2 Characterization techniques

4.2.1 Scanning electron microscopy

SEM and EDX measurements were conducted using a Quanta 3D FEG scanning electron microscope (FEI) to analyze the morphology of anode layers. For all measurements, the device was operated along with EDX using an acceleration voltage of 30 kV to also determine the elemental composition.

4.2.2 Optical profilimetry

Optical surface characterization was performed using a non-contact three-dimensional profilometer (SENSOFAR S Neox) operating in white light interferometry (WLI) mode. Topographical measurements were acquired over representative scan areas of 300×300 μm², 800×800 μm², and 1600×1600 μm². The technique provides nanometer-scale vertical resolution, while the lateral resolution depends on the selected objective lens (10×–50× magnification). For each sample, five independent regions were measured to ensure statistical reliability and representativeness. The interferometric data were processed using the instrument software (SensoMAP v10) to reconstruct the three-dimensional surface morphology and to extract quantitative roughness parameters, including the root-mean-square (Rq) height.

4.2.3 Atomic force microscopy

The surface of spray-coated anodes was examined using an AFM (TOSCA 400, Anton Paar Germany GmbH, Germany), which allows for the measurement of surface topography with atomic-scale resolution, i.e., 0.5 nm. A commercially available silicon tip was utilized, and the microscope was operated in 'Tapping mode', where the cantilever tip intermittently contacts and taps the sample surface.

4.2.4 Focused ion beam scanning electron microscopy

For determination of PC, the anode layer on Ni plate was mounted on a SEM sample holder using copper tape. A Helios NanoLab 600i SEM with a focused ion beam (FIB) was employed for cross-section imaging. A protective platinum line (15 µm x 0.5 µm, 0.5 µm thick) was deposited to shield the structure from high-energy FIBs. A rectangular area (15 µm x 15 µm) adjacent to the platinum line was selected, and a 5 µm deep hole was created using a 6.5 nA FIB beam current. The undamaged wall beneath the platinum deposition was polished with lower current ion beams (up to 93 pA) to obtain a smooth cross-section. Finally, images at various resolutions were captured using the SEM. The images obtained from the FIB-SEM device were processed using a MATLAB R2022a algorithm. The algorithm enhances image contrast to distinguish catalyst particles from pores, then binarizes the images into black (catalyst) and white (pores) pixels[56]. Porosity was calculated by determining the ratio of white pixels (pore area) to the total pixels, representing the PC of the anode layer.

4.2.5 Grazing-incidence X-ray diffraction

GIXRD measurements of the fabricated anode layers were performed using a Rigaku SmartLab diffractometer equipped with parallel-beam geometry and Cu Kα radiation ($\lambda = 1.5418$ Å). The instrument was operated at 40 kV and 50 mA. Diffraction patterns were recorded in ω–2θ scan mode over a 2θ range of 10–100° at fixed incidence angle of $\omega = 1.5°$, with a step size of 0.04° and a counting time of 1.2 s per step, resulting in a total acquisition time of approximately 45 min per sample. Phase identification was performed using Diffrac.Suite EVA V7.1 (Bruker) with reference patterns for Ni (#04-0850), Co (#15-0806), NiO (#65-2901), CoO (#74-2391), and Ni_3N (PDF#10-0280) obtained from the ICDD database.

4.2.6 Raman spectroscopy

Raman analyses of the nano-powders after ball milling were conducted using a DXR Raman microscope from Thermo Scientific. The excitation wavelength was 532 nm, and a laser power of 3 mW was employed to collect the Raman spectra.

4.2.7 X-ray photoelectron spectroscopy

XPS measurements were performed using a near ambient pressure XPS equipped with an Al-Kα source that produces monochromated X-rays of energy 1486.6 eV. After recording the survey scans using a pass energy of 100 eV, high resolution scans of all desired elements such as Ni, Co, and O were recorded applying a pass energy of 20 eV and a resolution of 0.05 eV. Data analysis was performed using the CasaXPS software.

4.3 Wettability and adhesion analysis

4.3.1 Contact angle measurements

Contact angle measurements were performed using OCA15PRO equipment (Data Physics Instruments GmbH). The measurements were conducted with 1 M KOH prepared with KOH pellets (Sigma-Aldrich, 85 %) as the liquid which was dropped on the sample surface at a dosing rate of 5 μL s^{-1}. Each measurement was performed in triplicate to ensure reproducibility.

4.3.2 Mechanical strength analysis

The mechanical strength of the various coatings was measured using the LUMiFrac centrifuge adhesion analyzer (LUM GmbH), which applies centrifugal forces to the coating using a copper test mass. The preparation of the Ni plates was carried out as follows. A stainless steel backplate was first cleaned manually with isopropanol, and the Ni plate was placed on top of the backplate, held in position by a strip of double-sided PET adhesive tape with an acrylic liner (Lohmann DuploCOLL 362.2). The catalyst layer on the Ni plate faced upwards. A round stainless-steel adapter (7 mm diameter) was then cleaned with isopropanol and glued onto the top of the catalyst layer. The copper test mass was placed on top of the adapter, such that the Ni plate with the catalyst layer was sandwiched between the backplate and the copper mass. This assembly was left to rest in fasteners for 24 hours, allowing sufficient contact for the pressure-sensitive adhesive to bond. After this, the assembly was inserted into an aluminum guiding sleeve, which ensured that all forces were applied perpendicularly, and then placed into the detector on the centrifugal plate. The detector recorded the frequency at which the copper test mass with the adapter detached from the catalyst layer, allowing the calculation of the adhesion strength based on the maximum centrifugal force and the adapter diameter. Three specimens were prepared for each variation in catalyst layer composition.

4.4 Electrochemical characterization

4.4.1 Operando Raman spectroscopy

Operando Raman measurements were performed using a commercial in situ Raman cell obtained from the online platform redox.me coupled with Raman spectroscopy from Oceanview with an excitation wavelength of 532 nm. The plasma-treated Ni-Co-O electrodes were used as the working electrode, Pt wire as the counter, and Ag/AgCl as the reference electrode in a three-electrode setup. The electrodes were preconditioned for 300 CVs in 1 M KOH at a scan rate of 100 mV s^{-1} prior to the recording of the Raman spectra. Afterward, a few CVs with lower scan rates were conducted to choose the potentials for the CP measurements during which Raman spectra were collected. Each potential was applied for 6 minutes, and Raman spectra were simultaneously recorded with an integration time of 1 minute in each case.

4.4.2 Beaker cell measurements

Electrochemical characterization was performed with Gamry potentiostats (Interface 1010E and Ref3000) in a 3-electrode beaker cell setup, similar to the design developed by Thissen et al., with a Hg/HgO reference and a glassy carbon counter electrode[57]. The reference electrode was regularly checked vs. a true RHE. The working electrode was the investigated materials, whereas the backside of the support was covered with an inert material, thus, the investigated geometrical electrode size was 1 cm^2. Measurements were done at RT in 200 mL of 1 M KOH. The Fe content in the electrolyte prior to each experiment was monitored and stayed constant for all experiments (200 ppb). The electrochemical protocol applied in this study was adopted from our previous work[37], and applied consistently to all samples. The detailed protocol can be found in Supplementary Information (**Section S9**).

Acknowledgements

The authors acknowledge financial support from the German Federal Ministry of Research, Technology and Space (BMFTR project "PrometH2eus", funding numbers 03HY105F and 03HY105A). We thank the University of Duisburg-Essen for Postdoc Seed Funding and Open Access funding enabled and organized by Projekt DEAL. The authors further acknowledge Dr. Ulrich Hagemann (Interdisciplinary Center for Analytics on the Nanoscale, ICAN) for

XPS measurements, Thai Binh Nguyen for FIB-SEM measurements, and Simon Heckenbach for adhesion testing.

Conflicts of Interest

The authors declare no conflicts of interest.

References

(1) Rai, P.; Gupta, P.; Saini, N.; Tiwari, A. K. Assessing the impact of renewable energy and non-renewable energy use on carbon emissions: evidence from select developing and developed countries. *Environ Dev Sustain* **2025**, *27* (2), 3059–3080. DOI: 10.1007/s10668-023-04001-6.

(2) Su, C. W.; Song, X. Y.; Dou, J.; Qin, M. Fossil fuels or renewable energy? The dilemma of climate policy choices. *Renewable Energy* **2025**, *238*, 121950. DOI: 10.1016/j.renene.2024.121950.

(3) Raza, M. A.; Aman, M. M.; Kumar, L.; Al-Khasawneh, M. A.; Faheem, M.; Ehyaei, M. A. Carbon neutrality and economic stability nexus: An integrated renewable energy transition to decarbonize the energy sector. *Energy Reports* **2025**, *13*, 4586–4608. DOI: 10.1016/j.egyr.2025.04.011.

(4) Yao, Y., Rui, X., Bai, R., Ouyang, Y., Li, G., Zhao, Y., ... & Yu, Y. Roadmap for next-generation electrochemical energy storage technologies: secondary batteries and supercapacitors. *ACS nano* **2025***, 19(34), 30568-30687.* DOI: 10.1021/acsnano.4c10091.

(5) Shanmugasundaram, S.; Thangaraja, J.; Rajkumar, S.; Denis Ashok, S.; Sivaramakrishna, A.; Shamim, T. A review on green hydrogen production pathways and optimization techniques. *Process Safety and Environmental Protection* **2025**, *197*, 107070. DOI: 10.1016/j.psep.2025.107070.

(6) Vincent, I.; Kruger, A.; Bessarabov, D. Hydrogen Production by water Electrolysis with an Ultrathin Anion-exchange membrane (AEM). *International Journal of Electrochemical Science* **2018**, *13* (12), 11347–11358. DOI: 10.20964/2018.12.84.

(7) Guo, S.; Lu, Q.; Zhou, X.; Wang, Y.; Li, M.; Liu, B. A Review of Ni-Based Electrode Materials for Electrocatalytic Oxygen Evolution Reaction. *Energy Fuels* **2025**, *39* (17), 7915–7940. DOI: 10.1021/acs.energyfuels.5c00255.

(8) Noh, W. Y.; Kazmouz, S. J.; Lee, S.; Peng, J.-K.; Shin, T. J.; Shviro, M. Decoupling electrode kinetics to elucidate reaction mechanisms in alkaline water electrolysis. *Energy Environ. Sci.* **2025.** DOI: 10.1039/D5EE03044G.

(9) Han, L.; Dong, S.; Wang, E. Transition-Metal (Co, Ni, and Fe)-Based Electrocatalysts for the Water Oxidation Reaction. *Advanced Materials* **2016**, *28* (42), 9266–9291. DOI: 10.1002/adma.201602270. Published Online: Aug. 29, 2016.

(10) Zou, F.; Manthiram, A. A Review of the Design of Advanced Binders for High‐Performance Batteries. *Advanced Energy Materials* **2020**, *10* (45), 2002508. DOI: 10.1002/aenm.202002508.

(11) Chandrasekaran, S.; Khandelwal, M.; Dayong, F.; Sui, L.; Chung, J. S.; Misra, R. D. K.; Yin, P.; Kim, E. J.; Kim, W.; Vanchiappan, A.; Liu, Y.; Hur, S. H.; Zhang, H.; Bowen, C. Developments and Perspectives on Robust Nano‐ and Microstructured Binder‐Free Electrodes for Bifunctional Water Electrolysis and Beyond. *Advanced Energy Materials* **2022**, *12* (23), 2200409. DOI: 10.1002/aenm.202200409.

(12) Le Roux, W. H.; Pfukwa, R.; Weigand, J. J.; Falch, A. A Comparative Study of Alternative Polymer Binders for the Hydrogen Evolution Reaction. *Electrocatalysis* **2025**, 1–18. DOI: 10.1007/s12678-025-00976-0.

(13) Kang, Y.; Deng, C.; Chen, Y.; Liu, X.; Liang, Z.; Li, T.; Hu, Q.; Zhao, Y. Binder-Free Electrodes and Their Application for Li-Ion Batteries. *Nanoscale Res Lett* **2020**, *15* (1), 112. DOI: 10.1186/s11671-020-03325-w.

(14) Chatwani, M.; Jain, A.; Marcks, C.; Johny, J.; Grebener, L.; Yun, H.; Khan, A. R.; Bendt, G.; Romeis, S.; Čolić, V.; Tesch, M. F.; Mechler, A. K.; Vinayakumar, V.; Segets, D. *Mechanochemical activation of nickel oxide: a pivotal step in the process chain enabling binder-free-anodes for alkaline water electrolysis*; Engineering Archive, 2025. DOI: 10.31224/4835.

(15) Koshy, S. S.; Rath, J.; Kiani, A. Fabrication of binder-less metal electrodes for electrochemical water splitting - A review. *Heliyon* **2024**, *10* (17), e37188. DOI: 10.1016/j.heliyon.2024.e37188.

(16) Ye, B., Cao, X., Zhao, Q., Zhou, A., & Wang, J. Free-standing NiCoSe2 nanostructure on Ni foam via electrodeposition as high-performance asymmetric supercapacitor electrode. *Nanotechnology* **2020***, 31(33), 335706.* DOI: 10.1088/1361-6528.

(17) Ishaq, M.; Jabeen, M.; Haider, R.; Nadir, K.; Ilyas, F.; He, Y.-S.; Che, H.; Khan, S.; Jiang, Y.; Zhao, S.; Ma, Z.-F. Geometric Design and Electronic Engineering of Transition Metal Phosphides for Key Electrochemical Energy Technologies: Nanoarchitectonics and Application. *Adv Funct Materials* **2025**, 2424141. DOI: 10.1002/adfm.202424141.

(18) Abbas, Q.; Khurshid, H.; Yoosuf, R.; Lawrence, J.; Issa, B. A.; Abdelkareem, M. A.; Olabi, A. G. Engineering of nickel, cobalt oxides and nickel/cobalt binary oxides by electrodeposition and application as binder free electrodes in supercapacitors. *Sci Rep* **2023**, *13* (1), 15654. DOI: 10.1038/s41598-023-42647-4.

(19) Bhoj, Pooja K., Rutuja A. Chavan, Seema A. Mane, Desta M. Ulisso, Jaeyeong Heo, I. W. P. Chen, Jyotiprakash B. Yadav, Tukaram D. Dongale, Bhaskar R. Sathe, and Anil V. Ghule. "Binder-free synthesis of nickel-iron-cobalt-oxide electrode for large-scale and durable oxygen evolution reaction." *International Journal of Hydrogen Energy 88* (**2024**): 604-616. DOI: 10.1016/j.ijhydene.2024.09.231.

(20) Darband, Ghasem Barati, Mahmood Aliofkhazraei, Suyeon Hyun, Alireza Sabour Rouhaghdam, and Sangaraju Shanmugam. "Electrodeposition of Ni–Co–Fe mixed sulfide ultrathin nanosheets on Ni nanocones: a low-cost, durable and high performance catalyst for electrochemical water splitting." *Nanoscale 11, no. 35* (2019): 16621-16634. DOI: 10.1039/C9NR04529E.

(21) Jiang, Si, Yong Yin, Yang Zhang, Zimeng Li, Shuai Guo, Yaogeng Lu, Zhaoxi Zhang, Tianle Zhu, Yifei Sun, and Xiang Li. "Plasma-assisted surface modification of heterogeneous catalysts: principles, characterization, and applications." *Catalysis Science & Technology 15, no. 19* (**2025**): *5635-5668*. DOI: 10.1039/d5cy00844a.

(22) Li, C.; Zhang, T.; Qiu, Z.; Ye, B.; Liang, X.; Liu, X.; Chen, M.; Xia, X.; Wang, C.; Wan, W.; Zhang, Y. Plasma‐assisted fabrication of multiscale materials for electrochemical energy conversion and storage. *Carbon Energy* **2025**, *7* (2), e641. DOI: 10.1002/cey2.641.

(23) Wagner, T.; Schaumburg, F.; Kensy, F.; Lorke, A.; Wöhrl, N. Changes: Optimizing morphology and chemistry of nickel surfaces by a scalable plasma process for hydrogen electrolyzers. *Surface and Coatings Technology* **2025**, *505*, 132056. DOI: 10.1016/j.surfcoat.2025.132056.

(24) Vinayakumar, Vineetha, et al. "Ni-Co-O anodes for the alkaline oxygen evolution reaction: Multistage electrode optimization and plasma-assisted activity enhancement enabled by a coherent workflow." *Chemical Engineering Journal (***2025***): 167169*. DOI: 10.1016/j.cej.2025.167169.

(25) Bapat, S.; Kilian, S. O.; Wiggers, H.; Segets, D. Towards a framework for evaluating and reporting Hansen solubility parameters: applications to particle dispersions. *Nanoscale Advances* **2021**, *3* (15), 4400–4410. DOI: 10.1039/D1NA00405K. Published Online: Jun. 17, 2021.

(26) Jain, A.; Vinayakumar, V.; Olean‐Oliveira, A.; Marcks, C.; Chatwani, M.; Mechler, A. K.; Andronescu, C.; Segets, D. From Small‐Area Observations to Insight: Surface‐Feature‐Extrapolation of Anodes for Alkaline Oxygen Evolution Reaction. *ChemCatChem* **2024**, *16* (5), e202301461. DOI: 10.1002/cctc.202301461.

(27) Gholami-Kermanshahi, M.; Lee, M.-C.; Lange, G.; Chang, S.-H. Effects of N 2 plasma modification on the surface properties and electrochemical performance of Ni foam electrodes for double-chamber microbial fuel cells. *Mater. Adv.* **2024**, *5* (13), 5554–5560. DOI: 10.1039/D4MA00153B.

(28) Manova, D.; Mändl, S.; Biermann, H.; Dalke, A. Surface segregation phenomena encountered during solid carbon active screen plasma nitrocarburizing of AISI 316L. *Surface and Coatings Technology* **2024**, *489*, 131091. DOI: 10.1016/j.surfcoat.2024.131091.

(29) Law, Y. T.; Dintzer, T.; Zafeiratos, S. Surface oxidation of NiCo alloy: A comparative X-ray photoelectron spectroscopy study in a wide pressure range. *Applied Surface Science* **2011**, *258* (4), 1480–1487. DOI: 10.1016/j.apsusc.2011.09.111.

(30) Sun, X.; Bao, J.; Li, K.; Argyle, M. D.; Tan, G.; Adidharma, H.; Zhang, K.; Fan, M.; Ning, P. Advance in Using Plasma Technology for Modification or Fabrication of Carbon‐Based Materials and Their Applications in Environmental, Material, and Energy Fields. *Advanced Functional Materials* **2021**, *31* (7), 2006287. DOI: 10.1002/adfm.202006287.

(31) Appleton, B. R. Ion bombardment modification of surfaces - fundamentals and applications. *Materials Science and Engineering* **1986**, *83* (1), 161. DOI: 10.1016/0025-5416(86)90183-7.

(32) Xiao, Y.; Zhang, P.; Zhang, X.; Dai, X.; Ma, Y.; Wang, Y.; Jiang, Y.; Liu, M.; Wang, Y. Bimetallic thin film NiCo–NiCoO 2 @NC as a superior bifunctional electrocatalyst for overall water splitting in alkaline media. *J. Mater. Chem. A* **2017**, *5* (30), 15901–15912. DOI: 10.1039/C7TA03629A.

(33) Jain, A.; Marcks, C.; Grebener, L.; Johny, J.; Odungat, A. S.; Chatwani, M.; Kräenbring, M.-A.; Shaji, A.; Tesch, M. F.; Mechler, A. K.; Vinayakumar, V.; Segets, D. A Proof‐of‐Principle Demonstration: Exploring the Effect of Anode Layer Microstructure on the Alkaline Oxygen Evolution Reaction. *Advanced Functional Materials* **2025**, *35* (19), 2421352. DOI: 10.1002/adfm.202421352.

(34) Wang, B.; Jiao, S.; Wang, Z.; Lu, M.; Chen, D.; Kang, Y.; Pang, G.; Feng, S. Rational design of NiFe LDH@Ni 3 N nano/microsheet arrays as a bifunctional electrocatalyst for overall water splitting. *J. Mater. Chem. A* **2020**, *8* (33), 17202–17211. DOI: 10.1039/D0TA01966F.

(35) Pandey, N.; Gupta, M.; Stahn, J. Study of reactively sputtered nickel nitride thin films. *Journal of Alloys and Compounds* **2021**, *851*, 156299. DOI: 10.1016/j.jallcom.2020.156299.

(36) Wu, C.; Sun, Y.; Liang, F.; Zhao, K.; Tang, H.; Tang, Y. Experimental and fractal analysis on wettability of rough structures. *Physics of Fluids* **2025**, *37* (1). DOI: 10.1063/5.0251042.

(37) Jain, A.; Marcks, C.; Mahler, G.; Odungat, A. S.; Grebener, L.; Johny, J.; Chatwani, M.; Shaji, A.; Melchert, T.; Tesch, M. F.; Behrens, M.; Mechler, A. K.; Vinayakumar, V.; Segets, D. *Wetting Across the Lyophilic–Lyophobic Spectrum: Morphological Tuning of Anode Catalyst Layers for the Alkaline Oxygen Evolution Reaction*; Engineering Archive, 2025. DOI: 10.31224/4749.

(38) Yue, B.; Chang, Z.; Wang, S.; Gao, X.; Guo, N.; Wang, Y.; Zhai, X.; Zhu, G. Wettability study of hydrophilic nickel coatings with high surface energy and high-

temperature wear resistance. *Materials Today Communications* **2023**, *34*, 105470. DOI: 10.1016/j.mtcomm.2023.105470.

(39) Tang, F.; Cheng, W.; Huang, Y.; Su, H.; Yao, T.; Liu, Q.; Liu, J.; Hu, F.; Jiang, Y.; Sun, Z.; Wei, S. Strong Surface Hydrophilicity in Co-Based Electrocatalysts for Water Oxidation. *ACS applied materials & interfaces* **2017**, *9* (32), 26867–26873. DOI: 10.1021/acsami.7b07088.

(40) Jiang, W.; Huang, X.; Ke, W.; Sheng, L.; Li, J.; Zhu, F.; Cheng, W.; Zhang, Z.; Lao, Y.; Chen, Y. Tuning wettability of nickel-based electrode by micro-nano surface structure to boost OER catalysis. *Journal of Alloys and Compounds* **2023**, *965*, 171367. DOI: 10.1016/j.jallcom.2023.171367.

(41) Qiu, Y.; Dai, X.; Wang, Y.; Ji, X.; Ma, Z.; Liu, S. The polyoxometalates mediated preparation of phosphate-modified NiMoO4-x with abundant O-vacancies for H2 production via urea electrolysis. *Journal of Colloid and Interface Science* **2023**, *629* (Pt A), 297–309. DOI: 10.1016/j.jcis.2022.08.145.

(42) Qiu, Y.; Zhang, Y.; Yu, M.; Li, X.; Wang, Y.; Ma, Z.; Liu, S. Ni—Co—O—S Derived Catalysts on Hierarchical N-doped Carbon Supports with Strong Interfacial Interactions for Improved Hybrid Water Splitting Performance. *Small* **2024**, *20* (29), e2310087. DOI: 10.1002/smll.202310087. Published Online: Mar. 26, 2024.

(43) Bhandari, S.; Schierholz, R.; Eichel, R.-A.; Luna, A. L.; Mechler, A. K. Exploring the Effect of Ball Milling on the Physicochemical Properties and Oxygen Evolution Reaction Activity of Nickel and Cobalt Oxides. *Adv Energy and Sustain Res* **2024**, *5* (12), 2400183. DOI: 10.1002/aesr.202400183.

(44) Li, Y.; Hu, L.; Zheng, W.; Peng, X.; Liu, M.; Chu, P. K.; Lee, L. Y. S. Ni/Co-based nanosheet arrays for efficient oxygen evolution reaction. *Nano Energy* **2018**, *52*, 360–368. DOI: 10.1016/j.nanoen.2018.08.010.

(45) Obradović, M. D.; Gojković, S. L. Challenges in determining the electrochemically active surface area of Ni-oxides in the oxygen evolution reaction. *Journal of Electroanalytical Chemistry* **2022**, *918*, 116479. DOI: 10.1016/j.jelechem.2022.116479.

(46) Cossar, E.; Houache, M. S.; Zhang, Z.; Baranova, E. A. Comparison of electrochemical active surface area methods for various nickel nanostructures. *Journal of Electroanalytical Chemistry* **2020**, *870*, 114246. DOI: 10.1016/j.jelechem.2020.114246.

(47) Qiu, Z.; Tai, C.-W.; Niklasson, G. A.; Edvinsson, T. Direct observation of active catalyst surface phases and the effect of dynamic self-optimization in NiFe-layered double hydroxides for alkaline water splitting. *Energy Environ. Sci.* **2019**, *12* (2), 572–581. DOI: 10.1039/C8EE03282C.

(48) Huang, J.; Zhang, Z.; Spezzati, C.; Clark, A. H.; Hales, N.; Genz, N. S.; Daffé, N.; Skoupy, R.; Gubler, L.; Castelli, I. E.; Schmidt, T. J.; Fabbri, E. Directly synthesized cobalt oxyhydroxide as an oxygen evolution catalyst in proton exchange membrane water electrolyzers. *Nat Commun* **2025**, *16* (1), 7518. DOI: 10.1038/s41467-025-62744-4.

(49) Lee, W. H.; Han, M. H.; Ko, Y.-J.; Min, B. K.; Chae, K. H.; Oh, H.-S. Electrode reconstruction strategy for oxygen evolution reaction: maintaining Fe-CoOOH phase with intermediate-spin state during electrolysis. *Nat Commun* **2022**, *13* (1), 605. DOI: 10.1038/s41467-022-28260-5. Published Online: Feb. 1, 2022.

(50) Ma, X.; Chang, Y.; Zhang, Z.; Tang, J. Forest-like NiCoP@Cu 3 P supported on copper foam as a bifunctional catalyst for efficient water splitting. *J. Mater. Chem. A* **2018**, *6* (5), 2100–2106. DOI: 10.1039/C7TA09619D.

(51) Barati Darband, G.; Aliofkhazraei, M.; Rouhaghdam, A. S. Facile electrodeposition of ternary Ni-Fe-Co alloy nanostructure as a binder free, cost-effective and durable electrocatalyst for high-performance overall water splitting. *Journal of Colloid and Interface Science* **2019**, *547*, 407–420. DOI: 10.1016/j.jcis.2019.03.098. Published Online: Mar. 29, 2019.

(52) Hemmati, K.; Moradlou, O.; Moshfegh, A. Z. Enhanced water oxidation reaction by binder-free nickel oxide nanorod arrays electrocatalyst. *International Journal of Hydrogen Energy* **2024**, *52*, 457–468. DOI: 10.1016/j.ijhydene.2023.07.040.

(53) Shi, J.; Hu, J.; Luo, Y.; Sun, X.; Asiri, A. M. Ni 3 Se 2 film as a non-precious metal bifunctional electrocatalyst for efficient water splitting. *Catal. Sci. Technol.* **2015**, *5* (11), 4954–4958. DOI: 10.1039/C5CY01121C.

(54) Zhou, J.; Yu, L.; Zhou, Q.; Huang, C.; Zhang, Y.; Yu, B.; Yu, Y. Ultrafast fabrication of porous transition metal foams for efficient electrocatalytic water splitting. *Applied Catalysis B: Environmental* **2021**, *288*, 120002. DOI: 10.1016/j.apcatb.2021.120002.

(55) Bapat, S.; Segets, D. Sedimentation Dynamics of Colloidal Formulations through Direct Visualization: Implications for Fuel Cell Catalyst Inks. *ACS Appl. Nano Mater.* **2020**, *3* (8), 7384–7391. DOI: 10.1021/acsanm.0c01467.

(56) Odungat, A. S.; Grebener, L.; Pasdag, O.; Nguyen, T. B.; Zhu, Y.; Kohsakowski, S.; Radev, I.; Özcan, F.; Segets, D. A Multiscale Pore Analysis Method for Polymer Electrolyte Membrane Fuel Cell Catalyst Layers Validated and Exemplified by Correlating Microstructure with Production Process Parameters. *Adv Energy and Sustain Res* **2025**, *6* (11), 2500043. DOI: 10.1002/aesr.202500043.

(57) Thissen, N.; Hoffmann, J.; Tigges, S.; Vogel, D. A. M.; Thoede, J. J.; Khan, S.; Schmitt, N.; Heumann, S.; Etzold, B. J. M.; Mechler, A. K. Industrially Relevant Conditions in Lab‐Scale Analysis for Alkaline Water Electrolysis. *ChemElectroChem* **2024**, *11* (1), e202300432. DOI: 10.1002/celc.202300432.

Supplementary Information

S1 Transmittogram

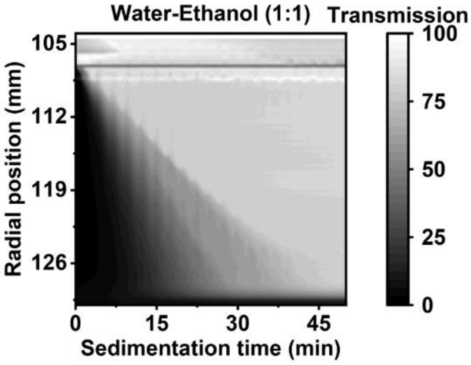

Figure S1 Transmittogram for Ni-Co-O in ethanol-water mixture done by converting the transmission profiles to 3-D plot.

S2 Optical profilometry

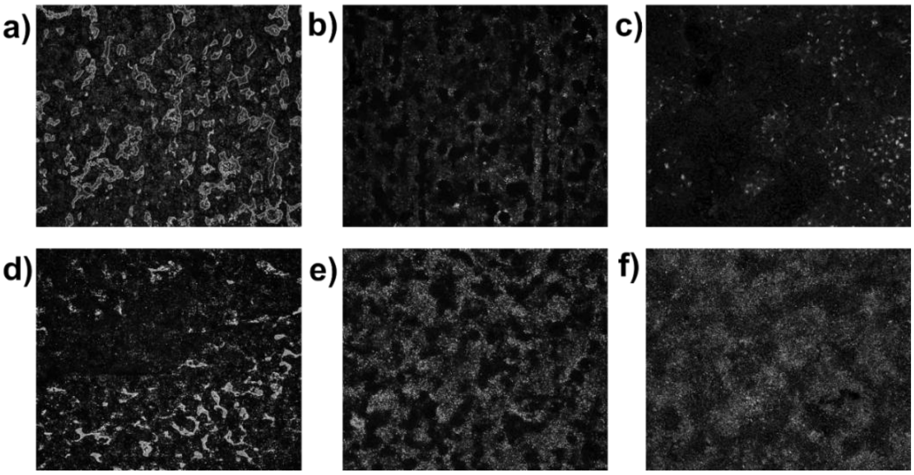

Figure S2 Optical profilometry images of Ni-Co-O anodes fabricated via spray coating on Ni plate substrates with varying numbers of deposition layers: a) 40L, b) 80L, and c) 120L. Corresponding images after PT are shown in d), e), and f), respectively.

S3 Surface features quantification

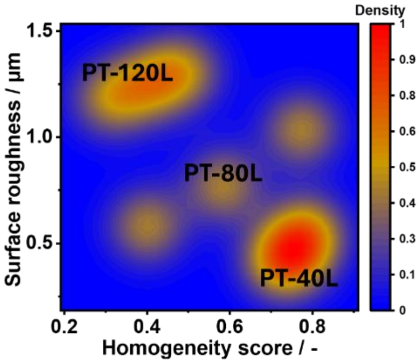

Figure S3 2-D correlation plot of surface roughness and homogeneity score derived from multi-stage data quantification (MSDQ) analysis of AFM images.

S4 Pore size distribution

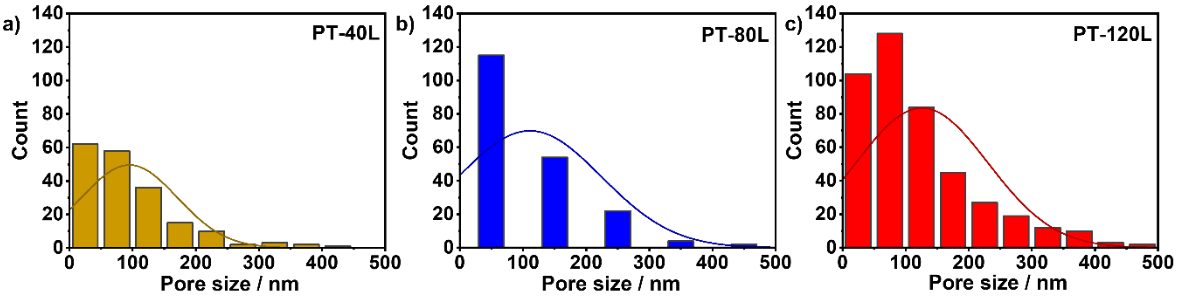

Figure S4 Pore size distribution from FIB-SEM analysis based on binary images for a) PT-40L, b) PT-80L, and c) PT-120L.

S5 Deconvoluted XPS spectra

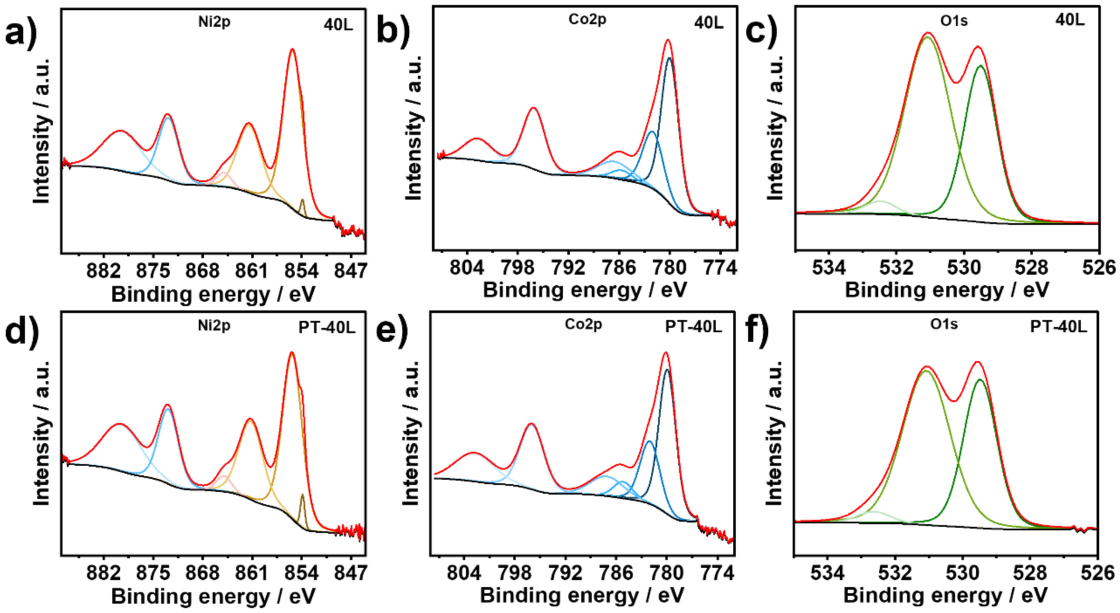

Figure S5.1 XPS deconvoluted spectra of the 40L sample showing a) Ni2p, b) Co2p, and c) O1s spectra. For the PT-40L anode, the corresponding spectra are shown for d) Ni2p, e) Co2p, and f) O1s.

Table S1. Raw data from XPS analysis for 40L coated anode.

Name	Position	FWHM	Raw area	Area/(RSF*T*MFP)
O 1s	529.51	1.14	1253.63	47.21
O 1s	531.08	1.61	2044.97	76.97
O 1s	532.49	1.09	100.44	3.78
Co 2p	779.98	2.44	1839.56	8.95
Co 2p	782	2.84	838.84	4.08
Co 2p	785.65	2.86	138.6	0.67
Co 2p	786.5	4.7	405.82	1.97
Co 2p	796.05	3.04	958.9	4.64
Co 2p	802.72	4.01	443.59	2.14
Ni 2p	855.26	3.18	2603.3	10.65
Ni 2p	861.41	4.02	1397.69	5.7
Ni 2p	879.43	6.45	1315.35	5.33
Ni 2p	872.83	3.34	1083.07	4.4
Ni 2p	853.9	0.57	49.67	0.2
Ni 2p	865	2.5	182.19	0.74

Table S2. Raw data from XPS analysis for PT-40L coated anode.

Name	Position	FWHM	Raw Area	Area/(RSF*T*MFP)
O 1s	529.48	1.17	1143.8	43.07
O 1s	531.08	1.68	1703.74	64.13
O 1s	532.63	1.17	88.1	3.31
Co 2p	779.93	2.38	1777.48	8.64
Co 2p	782	2.76	895.37	4.35

Co 2p	785.19	2.66	227.6	1.11
Co 2p	787.11	4.7	477.19	2.32
Co 2p	795.97	3.36	1119.2	5.41
Co 2p	802.75	5.45	789.53	3.81
Ni 2p	855.32	3.26	2522.56	10.31
Ni 2p	861.2	4.03	1475.95	6.02
Ni 2p	879.48	6.57	1434.6	5.82
Ni 2p	872.85	3.35	1175.39	4.78
Ni 2p	853.89	0.71	110.75	0.45
Ni 2p	865	2.5	185.25	0.76

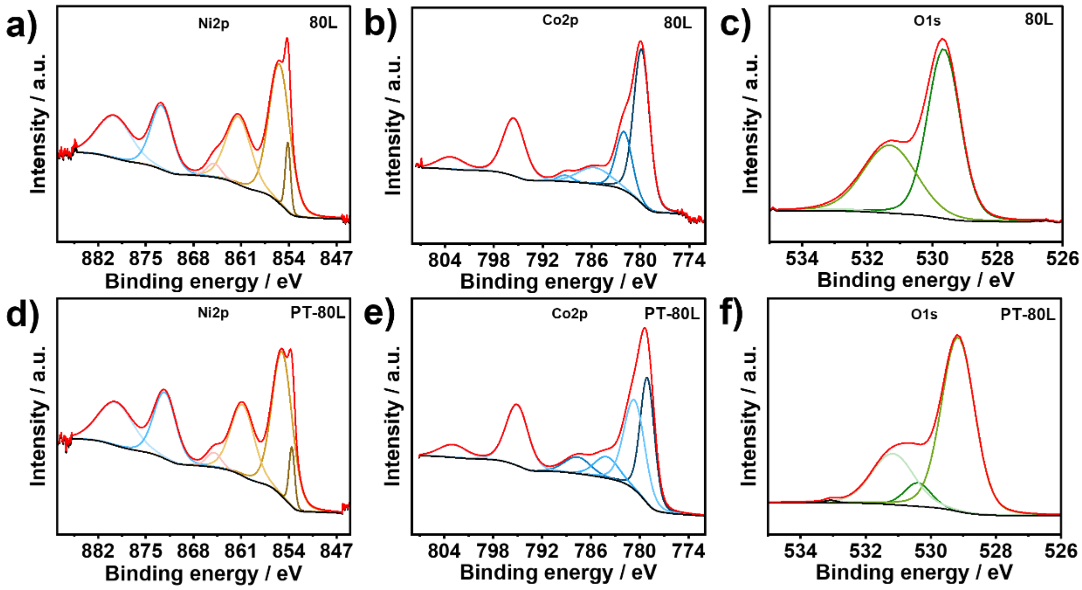

Figure S5.2 XPS deconvoluted spectra of the 80L sample showing a) Ni2p, b) Co2p, and c) O1s spectra. For the PT-80L anode, the corresponding spectra are shown for d) Ni2p, e) Co2p, and f) O1s.

Table S3. Raw data from XPS analysis for 80L coated anode.

Name	Position	FWHM	Raw area	Area/(RSF*T*MFP)
O 1s	529.65	1.18	1755.48	66.11
O 1s	531.31	1.92	1142.41	43
O 1s	532.8	1.6	29.81	1.12
Co 2p	779.84	2.31	2589.47	12.59
Co 2p	782	2.29	978.34	4.76
Co 2p	789.27	2.14	96.81	0.47
Co 2p	785.64	4.7	564.79	2.74
Co 2p	795.54	3.19	1335.42	6.46
Co 2p	803	3.84	333.52	1.61
Ni 2p	855.4	3.63	2701.53	11.05
Ni 2p	861	4.34	1574.44	6.43
Ni 2p	879.66	5.92	1328.59	5.39
Ni 2p	873	3.75	1282.81	5.22

Ni 2p	854.15	0.9	333.86	1.37
Ni 2p	865	2.5	184.86	0.75

Table S4. Raw data from XPS analysis for PT-80L coated anode.

Name	Position	FWHM	Raw Area	Area/(RSF*T*MFP)
O 1s	529	1.16	1644.32	61.92
O 1s	530.87	1.78	885.75	33.34
O 1s	533	1.11	26.62	1
Co 2p	779.35	2.31	2988.01	14.53
Co 2p	782	2.99	826.37	4.02
Co 2p	781.1	2	480.93	2.34
Co 2p	786.32	5.56	985.15	4.78
Co 2p	795.07	3.18	1642.49	7.95
Co 2p	802.76	6.74	769.73	3.71
Ni 2p	855.05	3.43	1935.64	7.91
Ni 2p	861	4.28	1251.52	5.11
Ni 2p	880	7	1.243	5.04
Ni 2p	872	4.06	1101.73	4.48
Ni 2p	853.56	1.06	257.68	1.05
Ni 2p	865	2.5	182.84	0.75

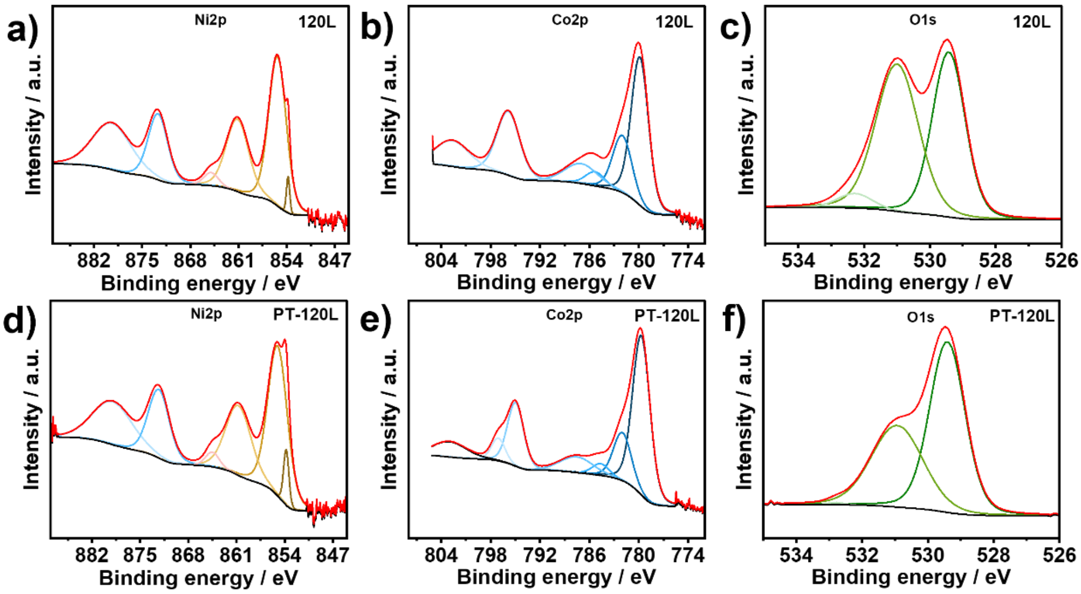

Figure S5.3 XPS deconvoluted spectra of the 120L sample showing a) Ni2p, b) Co2p, and c) O1s spectra. For the PT-120L anode, the corresponding spectra are shown for d) Ni2p, e) Co2p, and f) O1s.

Table S5. Raw data from XPS analysis for 120L coated anode.

Name	Position	FWHM	Raw Area	Area/(RSF*T*MFP)
O 1s	529.43	1.18	1408.51	53.03
O 1s	531	1.53	1626.05	61.2
O 1s	532.29	1.24	130.2	4.9
Co 2p	780	2.5	1966.91	9.57
Co 2p	782	3	831.76	4.04
Co 2p	785	2.76	207.75	1.01
Co 2p	787	4.7	495.46	2.4
Co 2p	795.84	3.29	1112.44	5.38
Co 2p	802.67	4.89	665.17	3.21
Ni 2p	855.34	3.01	2171.55	8.88
Ni 2p	861.15	3.85	1347.13	5.5
Ni 2p	879.42	6.57	1469.38	5.96
Ni 2p	872.69	3.33	1062.03	4.32
Ni 2p	853.81	0.55	98.1	0.4
Ni 2p	865	2.5	157.49	0.64

Table S6. Raw data from XPS analysis for PT-120L coated anode.

Name	Position	FWHM	Raw Area	Area/(RSF*T*MFP)
O 1s	529	1.27	1777.39	66.93
O 1s	531	2	1.234	46.44
O 1s	533	0.58	10.9	0.41
Co 2p	780	2.49	2880.45	14.01
Co 2p	782	2.51	879.27	4.27
Co 2p	784.58	2.38	204.81	0.99
Co 2p	787.5	4.7	541.52	2.63
Co 2p	795.15	2.72	1257.87	6.09
Co 2p	798	1.65	190.36	0.92
Ni 2p	855.03	3.35	1943.12	7.95
Ni 2p	861	4	1.176	5
Ni 2p	879	7	1.123	4.56
Ni 2p	872	3.63	958.98	3.9
Ni 2p	853.79	0.91	195.45	0.8
Ni 2p	865	2.37	133.55	0.54

S6 Depth profile XPS

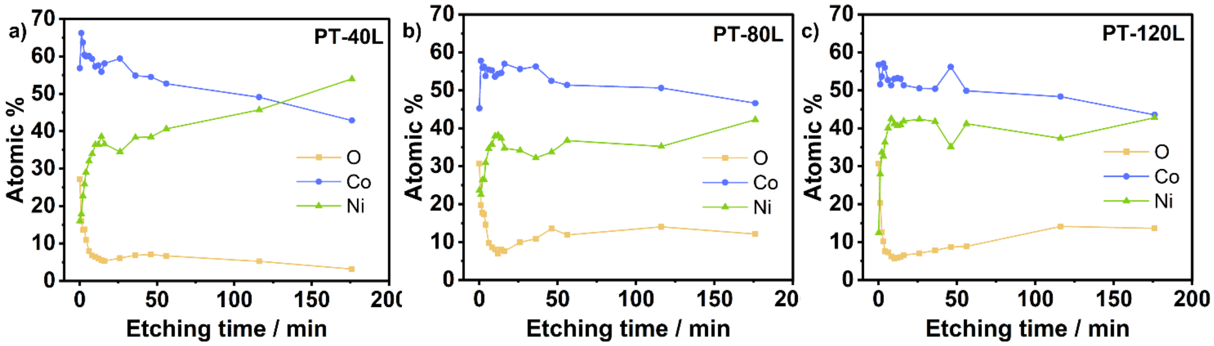

Figure S6 Elemental composition with respect to etching time from depth-profile XPS data for a) PT-40L, b) PT-80L, and c) PT-120L.

S7 Mechanical strength analysis

Table S7. Raw data for the adhesion strength analysis in MPa units.

Anode	PT-40L	PT-80L	PT-120L
Sample 1	2.15	1.71	0.76
Sample 2	1.02	1.44	1.06
Sample 3	1.85	1.13	1.32

S8 Operando Raman reversibility analysis

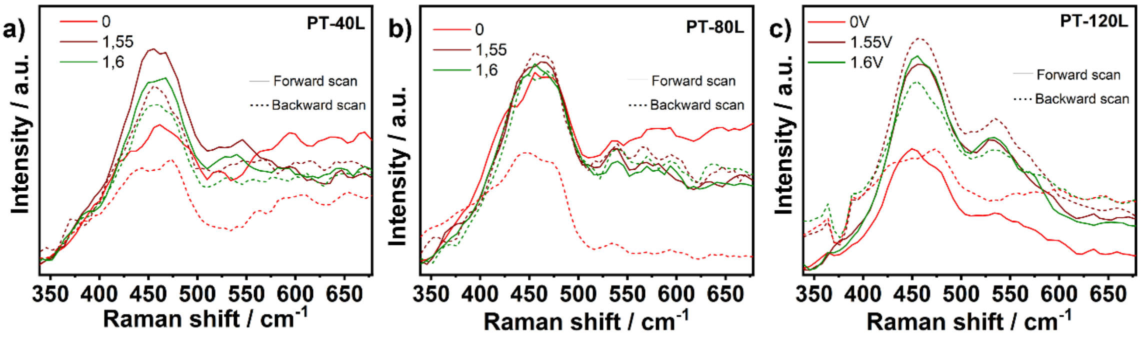

Figure S8 Operando Raman spectra showing forward (anodic) and backward (cathodic) potential scans for (a) PT-40L, (b) PT-80L, and (c) PT-120L. The nearly overlapping spectral features confirm the reversible evolution of surface species within the investigated OER potential window.

S9 Beaker cell analysis

Each experiment began with an initial conditioning step in which the anode potential was cycled 50 times between 0.25 and 1.5 V vs. RHE to activate redox-active surface species. After conditioning, the electrochemical response associated with surface redox processes was evaluated by integrating the redox charge from the cyclic voltammetry profiles. This charge was used as a relative measure of active surface area. In addition, PEIS was conducted at selected potentials between 0.9 and 1.6 V vs. RHE to characterize resistance contributions.

To assess activity and operational stability, the electrodes were subjected to four consecutive repetitions of a combined activity–stability sequence. Dynamic activity was first evaluated by cycling the potential three times between 1.0 and 1.8 V vs. RHE. Subsequently, stationary polarization measurements were performed by holding the electrode at stepwise increasing potentials from 1.0 to 1.8 V vs. RHE (1.0, 1.1, 1.2, 1.3, 1.4, 1.45, 1.5, 1.55, 1.6, 1.65, 1.7, 1.75, and 1.8 V), recording the current for 180 s at each step.

Stability was investigated via CP measurements at a constant current density of 100 mA cm^{-2} for 120 min per sequence. This stability test was repeated four times, resulting in a total operation time of 480 min. Before each major protocol block, the ohmic resistance (R_u) was determined by impedance spectroscopy at open-circuit potential using a 10 mV (rms) AC perturbation in the frequency range from 300 kHz to 1 kHz (10 points per decade). The resistance value was taken where a minimal phase deviation from zero was observed. All reported potentials were corrected using 100% iR compensation based on the respective R_u value.

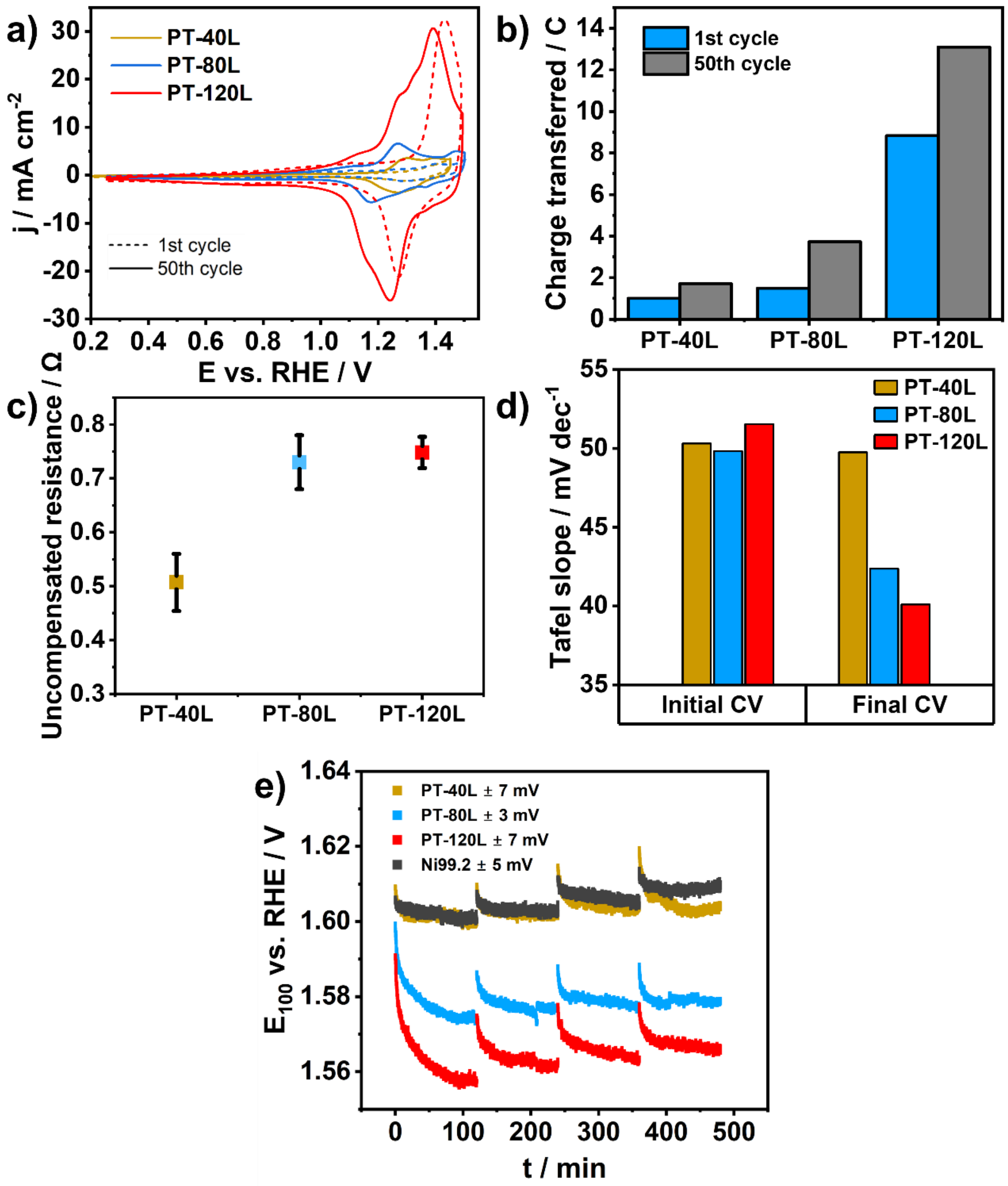

Figure S9 a) Electrochemical conditioning of plasma-treated Ni-Co-O anodes within a potential window of 0.2-1.45 V vs. RHE. Dashed lines correspond to the 1st CV cycle, while solid lines represent the 50th cycle, recorded at a scan rate of 100 mV s^{-1}. b) Quantified charge transfer extracted from the conditioning profiles for the 1st and 50th cycles. c) Uncompensated resistance (R_u) between the electrolyte, anode layer, and metallic support, measured at open-circuit potential. d). Tafel slope data derived from initial and final CV cycles. e) Chronopotentiometry (CP) measurements conducted at 100 mA cm^{-2} in 1 M KOH for plasma-treated samples and the Ni99.2 reference electrode over 480 min